

Molecular Cloud Evolution IV: Magnetic Fields, Ambipolar Diffusion, and the Star Formation Efficiency

Enrique Vázquez-Semadeni^{1*}, Robi Banerjee^{2†}, Gilberto C. Gómez^{1‡},
Patrick Hennebelle^{3§}, Dennis Duffin^{4¶}, and Ralf S. Klessen^{2||}

¹ *Centro de Radioastronomía y Astrofísica, Universidad Nacional Autónoma de México, Campus Morelia, Apdo. Postal 3-72, Morelia, 58089, México*

² *Zentrum für Astronomie der Universität Heidelberg, Institut für Theoretische Astrophysik, 69120 Heidelberg, Germany*

³ *Laboratoire de radioastronomie millimétrique (UMR 8112 CNRS), École Normale Supérieure et Observatoire de Paris, 24 rue Lhomond, 75231 Paris*

⁴ *Department of Physics and Astronomy, McMaster University, Hamilton, Ontario L8S 4M1, Canada*

20 November 2018

ABSTRACT

We investigate the formation and evolution of giant molecular clouds (GMCs) by the collision of convergent warm neutral medium (WNM) streams in the interstellar medium, in the presence of magnetic fields and ambipolar diffusion (AD), focusing on the evolution of the star formation rate (SFR) and efficiency (SFE), as well as of the mass-to-magnetic-flux ratio (M2FR) in the forming clouds. We find that: 1) Clouds formed by supercritical inflow streams proceed directly to collapse, while clouds formed by subcritical streams first contract and then re-expand, oscillating on the scale of tens of Myr. 2) Our suite of simulations with initial magnetic field strength of 2, 3, and 4 μG show that only supercritical or marginal critical streams lead to reasonable star forming rates. This result is not altered by the inclusion of ambipolar diffusion. 3) The GMC’s M2FR is a generally increasing function of time, whose growth rate depends on the details of how mass is added to the GMC from the WNM. 4) The M2FR is a highly fluctuating function of position in the clouds. This implies that a significant fraction of a cloud’s mass may remain magnetically supported, while SF occurs in the supercritical regions that are not supported. 5) In our simulations, the SFE approaches stationarity, because mass is added to the GMC at a similar rate at which it converts mass to stars. In such an approximately stationary regime, we find that the SFE provides a proxy of the supercritical mass fraction in the cloud. 6) We observe the occurrence of buoyancy of the low-M2FR regions within the gravitationally-contracting GMCs, so that the latter naturally segregate into a high-density, high-M2FR “core” and a low-density, low-M2FR “envelope”, without the intervention of AD.

Key words: interstellar matter – magnetic fields – stars: formation – turbulence

1 INTRODUCTION

Magnetic fields in molecular clouds (MCs), and the gradual redistribution of magnetic flux within them by ambipolar diffusion (AD), have been thought to be crucial ingredients in regulating star formation (SF) and its efficiency (SFE) for over two decades (see, e.g., the reviews by Shu et al. 1987; Mouschovias 1991, and references therein). In early studies,

MCs were considered to generally have strongly magnetically subcritical mass-to-flux ratios (M2FRs), and supercritical clouds were believed to be rare (e.g., Mouschovias 1991, sec. 2.1) so that the time for AD to allow their cores to become supercritical turned out to be very long, of order 10-20 times larger than the clouds’ free-fall time (t_{ff}) (e.g., Ciolek & Mouschovias 1994; Basu & Mouschovias 1994). In this “standard model” of magnetically-supported, AD-mediated subcritical clouds, the general mechanism for the formation of low-mass stars was through the slow gravitational contraction of isolated cores containing a very small fraction of the clouds’ mass, thus accounting for the very low observed global SFE of giant MCs (GMCs) (Myers et al. 1986; Evans et al. 2009).

However, subsequent studies have suggested that both

* E-mail: e.vazquez@crya.unam.mx

† E-mail: banerjee@ita.uni-heidelberg.de

‡ E-mail: g.gomez@crya.unam.mx

§ patrick.hennebelle@lra.ens.fr

¶ duffindf@mcmaster.ca

|| E-mail: rklessen@ita.uni-heidelberg.de

MCs (McKee 1989) and their clumps (Bertoldi & McKee 1992; Myers & Goodman 1988; Crutcher 1999; Bourke et al. 2001; Crutcher et al. 2003; Troland & Crutcher 2008) are close to being magnetically critical, with a moderate preference for being supercritical. This implies that, if a MC is subcritical, it is expected to be only moderately so as well, in which case the time for cores within it to become locally supercritical may be almost as short as the cores' free-fall time (Ciolek & Basu 2001; Vázquez-Semadeni et al. 2005). Moreover, MCs are generally believed to be supersonically turbulent (see, e.g., the reviews by Vázquez-Semadeni et al. 2000; Mac Low & Klessen 2004; Elmegreen & Scalo 2004; Ballesteros-Paredes et al. 2007; McKee & Ostriker 2007, and references therein), and in this case, AD must be treated nonlinearly. As a consequence, its characteristic timescale is expected to decrease, suggesting again that it may be comparable to the free-fall time (Fatuzzo & Adams 2002; Heitsch et al. 2004). Thus, the gravitational contraction and collapse of a star-forming region must occur rapidly, essentially in the timescales corresponding to those of a magnetically supercritical region, which is of the order of a few free-fall times (Ostriker et al. 1999; Heitsch et al. 2001; Vázquez-Semadeni et al. 2005; Galván-Madrid et al. 2007), although the subcritical envelope may still be held up by the magnetic field, since, at the envelopes' lower typical densities, the AD timescale is indeed much longer than the dynamical timescales.

Moreover, the realization that the majority of MCs may be supercritical, and that most stars, including low-mass ones, form in cluster-forming regions (Lada & Lada 2003), have forced a reconsideration of the problem, to accommodate the fact that the standard model's paradigm of low-mass star formation in strongly subcritical clouds may be the exception rather than the rule, even for the formation of low-mass stars.¹ Unfortunately, if most MCs are supercritical, one must once again face the old Zuckerman & Palmer (1974) conundrum that the Galactic star formation rate (SFR) should be roughly two orders of magnitude larger than the one observed, of $\sim 3\text{--}4M_{\odot} \text{ yr}^{-1}$ (see the supplementary material of Diehl et al. 2006). This is because globally supercritical clouds cannot be supported by the magnetic field, and thus should be collapsing as a whole.

Turbulence is often invoked as an additional source of support against the clouds' self-gravity, as if it were simply an extra source of pressure (Chandrasekhar 1951). Such a treatment, however, neglects the fundamental property of turbulence that the largest velocities occur at the largest scales, a property which is reflected in Kolmogorov (1941)'s famous energy spectrum of the turbulence. Studies taking this into account have generally only considered it from the point of view of the energetics involved (e.g., Bonazzola et al. 1987; Vázquez-Semadeni & Gazol 1995), but have neglected the vector nature of the velocity field. Having the largest velocity differences at the largest scales implies that the effect of classical vortical turbulence within a cloud or clump should be primarily to distort it, rather than support it (Ballesteros-Paredes et al. 1999a). In highly supersonic turbulence, Vázquez-Semadeni et al. (2008) have

recently noted that the non-thermal motions within clumps must contain a significant compressive component, even if the driving is purely solenoidal. This compressive component, rather than opposing gravity, aids it or is driven by it. This is consistent with recent suggestions that, for example, the Orion A cloud is collapsing, and producing the Orion Nebula Cluster (ONC) in the process (Hartmann & Burkert 2007), that the non-thermal motions within the clump NGC 2264-C correspond mainly to gravitational contraction, rather than to isotropic turbulence (Peretto, Hennebelle & André 2007), that massive star-forming regions may be immersed in large-scale accretion flows (Galván-Madrid et al. 2009; Csengeri et al. 2010; Schneider et al. 2010), and that MCs in the Large Magellanic Cloud seem to follow an evolutionary trend such that more evolved clouds are more massive (Fukui et al. 2009). Also, if the non-thermal motions within clouds were homogeneous and isotropic turbulence, it would be difficult to understand the common observation that SF occurs at localized spots within the clouds, rather than scattered throughout their volumes (e.g., Kirk et al. 2006; Evans et al. 2009).

These findings all suggest that an important, and perhaps even dominant, component of the nonthermal motions observed in MCs and their substructure is actually converging flows, which may be driven by gravity or by external compressions. In fact, a model in which the nonthermal motions in MCs are a gravitationally-driven mass cascade has been recently proposed by Field et al. (2008). Moreover, the collision of converging flows has been shown to produce turbulence in the compressed layers formed by them (Hunter et al. 1986; Vishniac 1994; Walder & Folini 2000; Heitsch et al. 2005, 2006; Vázquez-Semadeni et al. 2006). Klessen & Hennebelle (2010) have recently shown that the turbulent kinetic energy observed in objects as diverse as galactic disks, MCs, and protostellar accretion disks is in general consistent with being driven by infall from the environments of those objects. However, if the turbulence is being driven by the gravitational contraction, it cannot be expected to halt the contraction that drives it. Thus, one is faced with the Zuckerman-Palmer conundrum again.

One way to avoid the Zuckerman-Palmer conundrum is if large chunks of the molecular gas in the Galaxy are indeed magnetically subcritical and thus supported against gravity, while SF occurs precisely in those regions that are not, as recently suggested by Elmegreen (2007). Thus, the chaotic spatial and statistical distributions of the physical variables, produced by the turbulence in the forming MCs, may play a key role in the control of the SFR and the SFE.

In this paper we present numerical simulations of the formation and evolution of MCs, starting from their formation out of generic compressions in the warm neutral medium (WNM), and reaching up to their star-forming epochs, in the presence of magnetic fields and AD, in order to investigate the production of sub- and supercritical regions, and the rate at which clouds with various environmental conditions form stars. We focus on the effect of AD on the SFE and the global evolution of the clouds. The plan of the paper is as follows: in sec. 2 we present some general considerations on the evolution of the M2FR in MCs. In sec. 3 we present the numerical model and the parameters of the simulations. In sec. 4 we then present our results on the variability of the M2FR, the evolution of the SFE, and the role

¹ One instance of such an infrequent, strongly magnetized cloud may be the Taurus MC (Heyer et al. 2008)

of AD in the evolution of both sub- and supercritical clouds. Finally, sec. 5 presents a summary and our conclusions.

2 EVOLUTION OF THE M2FR IN MOLECULAR CLOUDS: FROM SUB- TO SUPERCRITICAL

Although the most commonly considered mechanism for increasing the M2FR of a certain density enhancement is the redistribution of magnetic flux among the central flux tubes of a cloud by AD (Mestel & Spitzer 1956; Mouschovias 1977), another important, yet often-neglected mechanism is that, for a uniform medium permeated by a given mean magnetic field strength B_0 , there is always a certain length along the field (termed the “accumulation length” by Mestel 1985; see also Shu et al. 2007) such that flux tubes longer than that contain enough mass per unit area to be magnetically supercritical. The criticality condition in terms of the mass column density $\Sigma = \rho L$ and the field strength B_0 for a cylindrical geometry is (Nakano & Nakamura 1978),

$$\Sigma/B_0 \approx (4\pi^2 G)^{-1/2} \approx 0.159 G^{-1/2}, \quad (1)$$

where ρ is the mass density and L is the cylinder length. This condition gives the accumulation length, in terms of fiducial values representative of the ISM in the solar neighborhood, as (Hartmann et al. 2001)

$$L_c \approx 470 \left(\frac{B_0}{5\mu\text{G}} \right) \left(\frac{n}{1\text{ cm}^{-3}} \right)^{-1} \text{ pc}, \quad (2)$$

where $n = \rho/(\mu m_H)$ is the number density of the medium, m_H is the Hydrogen mass, and μ is mean particle weight, taken as $\mu = 1.27$. In principle, if the Galactic field is primarily azimuthal, then the Galactic ISM at large is magnetically supercritical in general, because field lines do not end, and thus sufficiently long distances are always available along them.² Thus, *the M2FR of a system is not a uniquely defined, absolute parameter, but rather depends on where the system’s boundaries are drawn.* We also stress that the M2FR depends on the local geometry of the considered system. For instance, a system with spherical symmetry has a slightly lower critical value of $\mu_{\text{crit}} \approx 0.13 G^{-1/2}$ (Mouschovias & Spitzer 1976). Measuring the criticality of the streams with respect to this value would lead to a supercritical configuration for our runs B3 rather than sub-critical configurations.

Now consider a cloud or clump that is formed by the accumulation of gas along field lines in general.³ In the rest of this discussion, we will generically refer to the resulting density enhancement as a “cloud”, referring to either a cloud, a clump, or a core. Although redistribution of matter along field lines does not in principle affect the *total*

M2FR along the full “length” of a flux tube, this length is a rather meaningless notion, since the flux tube may extend out to arbitrarily long distances. What is more meaningful is the M2FR *of the dense gas that makes up the cloud*, since the cloud is denser than its surroundings, and thus it is the main source of the self-gravity that the field has to oppose. In fact, for the formation of a cloud out of flow collisions in the WNM, the cloud’s density is ~ 100 times larger than that of the WNM (Hennebelle & Pérault 1999; Koyama & Inutsuka 2002; Heitsch et al. 2005; Audit & Hennebelle 2005; Vázquez-Semadeni et al. 2006; Hennebelle et al. 2008; Banerjee et al. 2009), and so the latter’s self-gravity is negligible. Thus, in this problem, natural boundaries for the system are provided by the bounding surface of the dense gas, allowing a clear working definition of the M2FR.

However, contrary to the very common assumption of a constant cloud mass, the formation of clouds by converging gas streams implies that the cloud’s mass is a (generally increasing) function of time (Ballesteros-Paredes et al. 1999b; Vázquez-Semadeni et al. 2007; Vázquez-Semadeni et al. 2010; Banerjee et al. 2009; Klessen & Hennebelle 2010), a result that has recently received observational support (Fukui et al. 2009). This means that, *within the volume of the cloud, the M2FR is also an increasing quantity*, since the flux remains constant if the flow is along field lines, while the mass increases (see also Shu et al. 2007). If the cloud starts from essentially zero mass, this in turn implies that the M2FR of a cloud is expected to start out strongly subcritical (when the cloud is only beginning to appear), and to evolve towards larger values at later times. Rewriting eq. (2) for the column density, we see that the cloud becomes supercritical when

$$N_{\text{cr}} = 1.45 \times 10^{21} \left(\frac{B_0}{5\mu\text{G}} \right) \text{ cm}^{-2}, \quad (3)$$

where $N \equiv \Sigma/\mu m_H$ is the number column density along field lines.

The critical column density for magnetic criticality given by eq. (3) turns out to be very similar, at least for solar neighbourhood conditions, to the critical column density of hydrogen atoms necessary for cold atomic gas to become molecular, $N_H \sim 1\text{--}2 \times 10^{21} \text{ cm}^{-2}$ (e.g., Franco & Cox 1986; van Dishoeck & Black 1988; van Dishoeck & Blake 1998; Hartmann et al. 2001; Glover & Mac Low 2007a,b; Glover et al. 2010). Thus, *the evolution of a cloud is such that it starts out as an atomic and subcritical diffuse cloud (Vázquez-Semadeni et al. 2006) and, as it continues to accrete mass from the warm atomic medium, it later becomes molecular and supercritical, roughly at the same time* (Hartmann et al. 2001). This is fully consistent with the observation that diffuse atomic clouds are in general strongly subcritical (Heiles & Troland 2005), while MCs are approximately critical or moderately supercritical (Crutcher 1999; Bourke et al. 2001; Troland & Crutcher 2008).

Moreover, the critical column density given by eq. (3) is also very similar to that required for rendering cold gas gravitationally unstable, which is estimated to be

$$N_{\text{grav}} \approx 0.7 \times 10^{21} \left(\frac{P/k}{3000 \text{ K cm}^{-3}} \right)^{1/2} \text{ cm}^{-2} \quad (4)$$

² Note, however, that supercriticality does not necessarily imply collapse, since the gas may be thermally or otherwise supported, as is likely the case for the diffuse warm medium at scales of hundreds of parsecs.

³ Since compressions perpendicular to the magnetic field cannot induce collapse, and compressions oblique to the field can produce collapse by reorienting the directions of the flow and the field lines (Hennebelle & Pérault 2000), our assumed configuration involves no loss of generality.

(Franco & Cox 1986; Hartmann et al. 2001). Thus, at solar neighborhood conditions, a forming cloud is expected to become molecular, magnetically supercritical, and self-gravitating at roughly the same time.

It is important to note that the mass accretion onto a cloud due to gas stream collisions is likely to start along essentially just one dimension. This mode of mass accretion may be slow, and it has been argued that it may involve excessively long times (e.g., McKee & Ostriker 2007). However, numerical simulations of the process show that, once the gas has transitioned to the cold, dense phase, it soon becomes gravitationally unstable, even though it may remain mainly in the atomic phase, and three-dimensional gravitational contraction can then ensue, providing a much faster mode for increasing the column density (Vázquez-Semadeni et al. 2007; Elmegreen 2007; Heitsch & Hartmann 2008; Hennebelle et al. 2008; Banerjee et al. 2009). The same is true if the global convergence of the flow is driven by larger-scale gravitational instabilities (e.g., Kim et al. 2003; Li et al. 2005; Kim & Ostriker 2007). Of course, this increase of the column density due to gravitational contraction of the dense gas is only relevant to molecule formation. During such a process, the M2FR remains constant if the cloud’s mass remains fixed or varies on timescales much longer than the contraction, and the latter occurs under ideal MHD conditions. The gravitational contraction can only contribute to a further increase of the M2FR if the gravitational potential of the cloud causes it to accrete further amounts of diffuse gas, which transitions to the dense phase as it is incorporated into the bulk of the cloud.

In all of the processes discussed so far, AD has not played a role. This is of course due to the well known fact that AD is not dynamically relevant until densities as high as $n_{\text{AD}} \sim 10^5 \text{ cm}^{-3}$ are reached (Mouschovias et al. 1985). Such densities are only reached in the dense cores of MCs and therefore AD is not expected to cause any important effects on the global evolution of MCs. Such cores, however, may be magnetically subcritical if they form by turbulent compressions within the cloud before AD becomes locally important, even if the cloud is globally supercritical. This is because, under ideal MHD, a core formed within an initially uniform cloud must have a smaller M2FR than that of the cloud (Vázquez-Semadeni et al. 2005). In a sense, the core repeats the pattern followed by its parent cloud, initially being strongly subcritical and evolving towards higher values of the M2FR, being limited by the M2FR of its parent cloud, until AD becomes important and allows its M2FR to overtake that of the parent cloud, perhaps becoming supercritical and allowing the core to collapse. However, this notion has not been tested in the context of the global evolution of a GMC, in particular taking into account the property that the cloud’s M2FR should evolve (generally increasing) with time. In the remainder of the paper we investigate this scenario, by means of numerical simulations of the formation and evolution of a GMC, including AD, and focusing in particular on the resulting SFE. We are particularly interested in the star-forming properties of the cloud as it transits from sub- to supercritical.

3 THE NUMERICAL MODEL

3.1 The numerical code and setup

We use the adaptive mesh refinement (AMR) code FLASH (Fryxell et al. 2000) with MHD, modified to include the AD module developed by Duffin & Pudritz (2008). The AD treatment takes the single-fluid approximation, and uses a simple prescription to avoid the need to track the ion density in this approximation. This prescription essentially turns off AD at low ($n \lesssim 10^3 \text{ cm}^{-3}$) densities. For more details, we refer the reader to Duffin & Pudritz (2008).

The simulations also use a sink particle prescription (Bate et al. 1995; Jappsen et al. 2005; Banerjee et al. 2009; Federrath et al. 2010). A sink particle is created in a cell if the density there reaches a threshold density $n_{\text{sink}} = 2 \times 10^5 \text{ cm}^{-3}$, and the cell is a local minimum of the gravitational potential. When a cell forms a sink, the latter takes all the mass in excess of n_{sink} in the region where the density n satisfies $n \geq n_{\text{sink}}$. The sink particles have an accretion radius of 0.065 pc, corresponding to roughly 1 Jeans length at n_{sink} and $T \sim 20 \text{ K}$.

Concerning the heating and cooling, we use the same prescription used in Vázquez-Semadeni et al. (2007) and Banerjee et al. (2009), which is derived from the fit by Koyama & Inutsuka (2002) to the results of the chemistry and cooling calculations of Koyama & Inutsuka (2000). This prescription implies that the simulated ISM is thermally unstable in the density range $1 \lesssim n \lesssim 10 \text{ cm}^{-3}$, which, under thermal balance between heating and cooling, corresponds to the temperature range $5000 \gtrsim T \gtrsim 500 \text{ K}$.

We model the convergence of WNM flows as the collision of two large-scale cylindrical streams. Our setup is similar (though not identical) to the non-magnetic SPH simulation of Vázquez-Semadeni et al. (2007) labeled L256 Δv 0.17 (see their Fig. 1). Each stream is 112 pc long and has a radius of 32 pc. The streams collide at the plane $x = 0 \text{ pc}$, and are embedded in a $(256 \text{ pc})^3$ simulation box, in which the coordinates range from -128 to 128 pc . The numerical box is periodic, and the streams are completely contained within it, ending at a distance of 16 pc from the x boundaries. The resulting cloud occupies a relatively small volume far from the boundaries, and so it can interact freely with its diffuse environment, with relatively little effect from the boundaries. Most importantly, the cloud is free to grow by accretion from the WNM.

The cylindrical streams are given an initial, moderately supersonic inflow velocity v_{inf} so that they collide at the centre of the numerical box. The inflow speed of each stream is measured with respect to the isothermal sound speed of 5.7 km s^{-1} that corresponds to the initial temperature of 5000 K. This isothermal inflow Mach number is denoted \mathcal{M}_{inf} . We also add 10% random velocity perturbations to the bulk stream speeds, in order to trigger the instabilities that generate turbulence in the forming cloud (Vishniac 1994; Heitsch et al. 2005; Pittard et al. 2005; Vázquez-Semadeni et al. 2006). The box is initially filled with WNM at a uniform density of $n = 1 \text{ cm}^{-3}$ ($\rho = 2.12 \times 10^{-24} \text{ g cm}^{-3}$, using a mean atomic weight of 1.27). At the temperature of $T = 5000 \text{ K}$ for the warm phase, this implies that the cold phase comes into hydrostatic thermal pressure balance with the WNM at a density $n \approx 100 \text{ cm}^{-3}$ (see Fig. 2 of Vázquez-Semadeni et al. 2007). However, in our simu-

lations the density of the cold phase is higher, because it is in balance with the sum of the thermal and the ram pressure of the colliding streams (Vázquez-Semadeni et al. 2006; Hennebelle et al. 2008; Banerjee et al. 2009).

3.2 Resolution issues

We start our simulations at a base resolution of 512^3 , i.e. $\Delta x = 0.5$ pc, at the convergence point of the flows. Additionally, we allow the code to refine up to 4 additional levels, the highest of which corresponds to a maximum resolution of 8192 grid points, or a grid spacing of $\Delta x = 0.03$ pc in each direction. For the dynamical mesh refinement we use a Jeans-type criterion (Truelove et al. 1997, see, however, Federrath et al. (2011, submitted) for a more stringent criterion in the presence of magnetic fields), requiring the local Jeans length to be resolved with at least 10 grid cells while refining is active. Beyond the last refinement level, the Jeans length begins to be more poorly resolved, until a maximum allowed density of $n_{\text{sink}} = 2 \times 10^5 \text{ cm}^{-3}$ is reached, at which a sink particle is formed. We refer the reader to Banerjee et al. (2009) for a discussion of the justification and possible limitations of this choice with regards to thermal issues. Here we discuss issues related with gravity and AD.

The value of n_{sink} we use was chosen in order to reasonably ensure that the material going into sink particles is actually gravitationally bound. Indeed, Galván-Madrid et al. (2007) found that, when cores are defined by means of a density threshold, most cores defined by thresholds $\gtrsim 10^5 \text{ cm}^{-3}$ proceed to collapse. Instead, when cores are defined by lower thresholds (say, $\sim 10^4 \text{ cm}^{-3}$), a significant fraction of them is transient, rebounding instead of collapsing (see also Ballesteros-Paredes et al. 2003; Klessen et al. 2005; Vázquez-Semadeni et al. 2005). Now, at $n = n_{\text{sink}}$ and $T = 20$ K, the Jeans length is $L_J = 0.066$ pc, and so we marginally fail to fulfill the minimum Jeans criterion, of resolving L_J with at least 4 cells. However, this should not introduce any significant errors, as we are not concerned here with the fragmentation of the core into multiple stars, nor with their mass distribution, but only with the total mass going into stars.

Another issue is that numerical diffusion can have an effect similar to that of AD, as discussed by Klessen et al. (2000). Specifically, since the scale of the densest cores is a few grid cells, numerical diffusion can cause the magnetic flux to diffuse out of them, in a similar manner to AD. Indeed, we do occasionally observe the occurrence of gravitational collapse in magnetically subcritical, ideal MHD simulations, in which theoretically this should not occur. Moreover, since n_{sink} effectively constitutes an upper limit to the density that can be reached by any cell in the simulation, and since we have chosen a value of n_{sink} that is of the same order as n_{AD} , the highest densities in the code will be of the order of n_{AD} , and numerical diffusion and AD will have comparable effects. This limitation could be avoided by using an even larger number of refinement levels but, since the simulations are already very numerically expensive ($\sim 200,000$ CPU hours per run), this option is not presently feasible. Alternatively, we could give up on satisfying the Jeans criterion, simply raising n_{sink} without increasing the allowed number of refinement levels, an option that we may attempt elsewhere. In any case, the effect of numerical diffu-

sion will again be to allow SF to occur more readily than if mediated by AD alone in subcritical cases, and so our SFRs must again be considered upper limits to the ones caused by AD alone.

3.3 The simulations

We consider five numerical simulations with three reasonably realistic values of the initial, uniform magnetic field B_0 , of 2, 3, and 4 μG , respectively. These values span the observed range of values of the uniform component of the Galactic magnetic field (Beck 2001). The initial field is along the x -direction.

With respect to the cylindrical criticality criterion, eq. (1), these cases respectively correspond to $\mu/\mu_{\text{crit}} \approx 1.36$, 0.91 and 0.68, so that the first case is magnetically supercritical while the other two are subcritical. Note, however, that the subcritical cases are only so because of the finite extent (256 pc) of the numerical box. For $B_0 = 3$ and 4 μG , lengths of 280 and 380 pc, respectively, would be required to render the system magnetically critical. Also, because the critical value of the mass-to-flux ratio depends on the geometry of the considered configuration, individual (molecular) clumps could be supercritical if compared to the slightly lower μ_{crit} of Mouschovias & Spitzer (1976) (see discussion in Sec. 4.2).

The supercritical case is considered only in the AD regime, as we do not expect the absence of AD to make a significant difference in this case. The $B_0 = 3$ and 4 μG cases are considered both in the “ideal” and AD regimes, to investigate the effect of AD on the star-forming properties of magnetically subcritical clouds. Note that we have written the word “ideal” within quotation marks because we cannot avoid the effect of numerical diffusion, even if we turn off the AD. Except for the value of the magnetic field strength and whether AD is on or off, the simulations are otherwise identical, all having an inflow speed of 13.9 km s^{-1} , corresponding to an isothermal Mach number $\mathcal{M}_{\text{inf}} = 2.44$ with respect to the unperturbed, initial medium at $T = 5000$ K.

The runs are labeled mnemonically, so that the first two characters of the run’s name indicate the field strength in μG (e.g., “B3” denotes $B_0 = 3 \mu\text{G}$), and the last two denote whether the simulation is in the ideal MHD case (“MH”) or includes AD (“AD”). Table 1 summarizes the parameters used in each of the five runs. The last column in this Table gives the maximum time reached by each simulation.

3.4 Considerations on measuring the mass-to-flux ratio

In what follows, we will be presenting measurements of the M2FR in various regions of the simulations. However, this is not an unambiguous task in general, and in fact the M2FR can be measured using different procedures. In principle, the M2FR should be measured along flux tubes, in order for the measurement to be directly representative of the dynamical effect of the field on the gas. Thus, the measurement should be performed by tagging a bundle of field lines, and integrating the density along the path defined by them. Unfortunately, such a measurement is extremely difficult to perform, even in the simulations. A magnetic flux tube may lose

Table 1. RUN PARAMETERS

Run name	B_0 [μG]	AD	μ/μ_{crit}	Final time [Myr]
B2-AD	2.0	on	1.36	31.4
B3-MH	3.0	off	0.91	26.1
B3-AD	3.0	on	0.91	35.6
B4-MH	4.0	off	0.68	48.4
B4-AD	4.0	on	0.68	59.2

Table 2. Initial conditions and the final simulation time of the runs presented in this work. To calculate the magnetic critically of the entire system we use the critical mass-to-flux ratio, $\mu_{\text{crit}} \approx 0.16 \text{ G}^{-1/2}$, for a cylindrical geometry of Nakano & Nakamura (1978)

coherence if the field lines that compose it diverge from each other at long distances. Also, the field near and within the cloud can be significantly distorted, due both to the turbulence in the cloud, and to its gravitational contraction, even if the initial flow direction is along the field lines.

Observationally, the M2FR is often estimated by measuring the ratio of column density to magnetic field strength, N/B , along lines of sight (LOSs) through the cloud of interest (e.g. Crutcher et al. 2003). However, this procedure actually intersects many different flux tubes, and thus gives only an approximation to the actual M2FR of a single flux tube. As discussed by Crutcher (1999), if a cloud is flattened, its plane is perpendicular to the magnetic field lines, and the system is observed at an angle θ , then the observed M2FR, or equivalently, the N/B ratio, will be related to the actual one by $(N/B)_{\text{obs}} = N/(B \cos^2 \theta)$. Alternatively, as is the case for the measurements we present below, if the observation is performed along an LOS that is perpendicular to the cloud, but the magnetic field is at an angle θ with respect to the LOS and to the normal to the plane, then we have that $(N/B)_{\text{obs}} = N/(B \cos \theta)$, with $|\theta| \leq \pi/2$. In either case, $(N/B)_{\text{obs}}$ tends to overestimate the actual value, and on some occasions very large values may be artificially measured. This implies that a map of $(N/B)_{\text{obs}}$ is actually a map of *upper limits* to the actual N/B . This led Crutcher (1999) to introduce statistical correction factors of $1/2$ – $1/3$ to the set of M2FR values obtained in the observations he considered.

The equivalent procedure for the simulation data is to measure M2FR along LOSs through the clouds in our simulations. We choose the LOSs to lie along the x -direction, since this is the direction of the mean magnetic field and of the colliding WNM streams, and thus it is the direction along which the column density is dynamically relevant. Specifically, we then measure the M2FR as

$$\mu = \frac{\Sigma}{\langle B_x \rangle} \equiv \frac{\int_L \rho dx}{L^{-1} \int_L B_x dx}, \quad (5)$$

where L is the stretch of the cloud along the x direction. The path L is chosen so as to contain the full extent of the cloud’s thickness. This is done for every position on the plane of the cloud, to obtain maps of the M2FR over the cloud’s surface. We refer to this as “the projection method” of measuring the M2FR in the simulations.

In order to appreciate the amount of distortion that may be present in the field within the clouds, in Fig. 1 we show cross sections through the centre of runs B3-MH and B4-MH along the (x, y) plane, showing the density field and the component of the magnetic field on this plane. We observe that in run B3-MH the field lines are not strongly bent, except at the sites of local collapse. This suggests that the M2FRs we measure by the projection method should not exceedingly overestimate the actual flux-tube value.

Nevertheless, a more definite way to estimate the amount of overestimation of the M2FR incurred in by the projection method is to use a different estimator. One such estimator is what we call the “local method”, which consists in measuring the M2FR for individual cells in the simulations, using the total magnetic field strength. Specifically, we measure the gas mass M and read off the total magnetic field strength B in a cell, in order to calculate the M2FR as

$$\mu \approx \frac{M}{B dx^2}, \quad (6)$$

where dx is the cell’s side length. This estimator gives a lower bound to the M2FR in a magnetic flux tube, since it only counts the mass in a single cell within that tube. This method has no observational analogue but, by using the two methods, we expect to bracket the true distribution of values of the M2FR, at least in a statistical sense.

4 RESULTS

4.1 Global evolution and star formation

We first direct our attention to the global evolution of the clouds. The supercritical run B2-AD evolves very similarly to the non-magnetic runs presented by Vázquez-Semadeni et al. (2007) and Vázquez-Semadeni et al. (2010) and the strongly supercritical runs presented by Hennebelle et al. (2008) and Banerjee et al. (2009). The cloud starts out as a thin cylindrical sheet that fragments and thickens as time increases, until it becomes gravitationally unstable and begins a global radial contraction at $t \sim 9$ Myr. Shortly after that ($t \sim 12$ Myr) star formation begins in the densest fragments (“clumps”), while the fragments continue to fall towards the global centre of mass, and by $t \sim 24$ Myr a dense cloud of radius ~ 10 pc has formed there, which does not appear to contract further. This lack of contraction, however, is only apparent, because in fact gas is being consumed within the cloud by SF, and gas from the outside continues to fall onto the cloud. Figure 2 shows this run at $t = 10, 20$ and 30 Myr, illustrating its evolution.

On the other hand, the subcritical runs B3 and B4 undergo a period of initial contraction followed by a *rebound*, eventually settling into an oscillatory regime, which consists of alternating periods of contraction and expansion around the magnetostatic equilibrium state, as previously observed by Li & Nakamura (2004). These oscillations are best seen in animations of the simulations (not shown), but they can also be observed in Figs. 3 and 4, which show snapshots of the density field of runs AD-B3 and AD-B4 at various times, respectively. In Fig. 3, it can be seen that the central density is larger at the intermediate time shown in the *middle* panel than at the final time shown at the *right* panel. A similar

behavior is seen in Fig. 4, where the central density is seen to be larger at times $t = 20.5$ and $t = 48$ Myr than at $t = 34$ Myr. The B3 runs, having a weaker mean field, contract for a longer time (up to $t \sim 25$ Myr) and reach a smaller size (radius $R \sim 20$ pc) than the B4 runs (maximum contraction at $t \sim 20$ Myr, with radius $R \sim 25$ pc). The B4 runs, which were followed to longer times, clearly exhibit the oscillatory regime, with a period of ~ 30 Myr. The oscillations can also be seen in Fig. 5, which we now discuss.

Figure 5 shows, for all the runs, the evolution of the total dense gas mass and total sink mass (*top left panel*), the time derivative of the total sink mass \dot{M}_{sinks} (*top right panel*), the total number of sinks (*bottom left panel*), and the SFE (*bottom right panel*), defined as

$$\text{SFE}(t) = \frac{M_{\text{sinks}}(t)}{M_{\text{dense}}(t) + M_{\text{sinks}}(t)}, \quad (7)$$

where M_{dense} is the mass of the gas with density $n > 100 \text{ cm}^{-3}$, and M_{sinks} is the total mass in sink particles. We take \dot{M}_{sinks} as a proxy for the SFR.

The evolution of the runs is seen to depend sensitively on the magnetic field strength. For $t \gtrsim 7$ Myr, the dense gas mass oscillates by factors of 2–4 for the subcritical runs B3 and B4, in both the MHD and the AD cases, evidencing again the oscillatory regime in which these runs engage. The maxima of the mass in the subcritical runs coincide with the times of maximum compression. This may be partially an artifact of the threshold density we have chosen for defining the cold gas. Because the global magnetic support for the cloud prevents it from contracting much, the gravitational binding of the cloud is generally weak. This in turn means that the during periods of maximum expansion, a significant fraction of the cloud, although still in the cold phase, may be below the density threshold of 100 cm^{-3} we have used for defining the cloud. Nevertheless, if the mean density of the cloud varies, it is likely that the molecular fraction should actually vary as well, since molecular gas may be dissociated if the cloud’s column density decreases sufficiently (Glover et al. 2010). Thus, during periods of expansion, the cloud may contain a lower molecular fraction. In addition, significant amounts of gas may be in a transient state between the warm and cold phases of the ISM (see the reviews by Vázquez-Semadeni et al. 2003; Hennebelle et al. 2009; Vázquez-Semadeni 2009, and references therein), being thus lost from the cold, dense phase.

The supercritical run B2, on the other hand, does not exhibit such strong oscillations in its dense gas mass content. Instead, the dense gas mass increases rapidly at first. This is because this run does not engage in any radial oscillations, but simply proceeds directly to collapse. Interestingly, however, the dense gas mass later becomes roughly stationary, although this stabilization is not due to the cloud being in any sort of equilibrium, but rather to the fact that it is forming stars at roughly the same rate it accretes mass from the WNM. Indeed, the *red lines* in the *top left panel*, as well as the *top right panel* of Fig. 5 show that the total sink mass in the simulation increases at a steady pace, of roughly $400 M_{\odot} \text{ Myr}^{-1}$ during the time interval $20 < t < 30$ Myr.

All runs, including those that are subcritical, form “stars” (i.e., sink particles), since, as discussed in Sec. 3.2, numerical diffusion acts in a similar manner to AD. Nevertheless, when AD is included the total sink number and mass

increase, the dense gas mass decreases, these effects being relatively more noticeable for the strong-field runs B4. In general, as can be seen from the *bottom left panel* of Fig. 5, the total number of sinks in the B4 and B3 cases is larger only by a few sinks when AD is included. This reinforces our conclusion from Sec. 3.2 that numerical diffusion has an effect of comparable strength to that of AD in our simulations, since AD is able to induce the collapse of a few clumps in addition to those that collapse because of numerical diffusion. In the case of the B3 runs, the relative effect of AD is smaller because the same difference of a few extra sink particles is a smaller fraction of the total number of sinks produced.

Indeed, run B3-AD forms stars at a much higher rate than run B4-AD, even though both are subcritical. The time derivative of the sink mass, \dot{M}_{sinks} , in run B3-AD is roughly one order of magnitude larger than that of run B4-AD, as seen in the *top right panel* of Fig. 5. In fact, the formation of sinks completely stops in run B4-AD after $t \approx 27$, as can be seen in the *bottom left panel* of this figure. The very slight increase in the sink mass observed during this period (*top left panel, dash-dotted red line*) is due to accretion onto the existing sink particles, rather than to the formation of new particles. Run B2-AD, on the other hand, is seen to have a larger SFR than run B3-AD, although only by factors of a few. Also, it can be seen from all panels of Fig. 5 that the onset of SF is delayed as B_0 is increases, but that the presence of AD shortens this delay. It is important to note that all SF in the runs occurs *after* the cloud has been assembled and its M2FR has reached a nearly stationary value ($t > 10$ Myr).

To conclude this section, the *bottom right panel* of Fig. 5 shows the evolution of the SFE, defined by eq. (7), in all simulations. Again, a continuous trend of increasing SFE with decreasing B_0 is observed throughout our set of simulations. The supercritical run B2-AD reaches an SFE of $\sim 35\%$ at $t = 30$ Myr. For comparison, at this time, run B3-AD has reached an SFE of $\sim 25\%$, while run B4-AD has reached only $\text{SFE} \sim 3\%$. Although at face value these numbers would suggest that run B4-AD compares best to the observed SFEs of GMCs (Myers et al. 1986; Evans et al. 2009), this conclusion may be premature, since the additional effect of stellar feedback in reducing the SFE (e.g., Vázquez-Semadeni et al. 2010) is not taken into account in the present simulations. We conclude that the SFR and the SFE can depend sensitively on the mean field strength, even for globally subcritical cases, and that the marginally subcritical run has an SFE comparable to that of the supercritical case.

4.2 Spatial and probability distribution of the mass-to-flux ratio

A key piece of information needed to understand the behavior of simulations is the spatial distribution of the M2FR, as well as the evolution of its global average value. In what follows, we discuss the M2FR estimated using the projection method (cf. eq. [5]) along LOSs parallel to the x axis (i.e., perpendicular to the plane of the cloud), taking L as the path $-10 < x < 10$ pc along the direction of the inflows. We consider the M2FR normalized to the critical value given by eq. (1). Given the flattened geometry of our clouds, we consider that this is a more realistic value of the critical

M2FR than the other commonly encountered critical value of $(6\pi^2 G)^{-1/2} \approx 0.13 G^{-1/2}$, which holds for spherical geometry (e.g., Shu 1992). Figure 6 shows snapshots of the normalized M2FR for runs B2-AD, B3-AD and B4-AD in the *top row*, and of runs B3-MH and B4-MH in the *bottom row*, all at $t = 20$ Myr. In all cases, the spatial distribution of the M2FR is seen to fluctuate strongly.

Comparing the MH and AD cases, it is interesting to note that the spatial structure of the M2FR is similar in the large-scale features, but differs in the shape and precise location of the fine, small-scale ones. This is a manifestation of the system being chaotic, so that the subtle variations in the magnetic forces at the densest structures induced by AD are sufficient to change the details in the topology of the gas. Presumably, for sufficiently long times the differences in structure will reach even the largest scales. On the other hand, simple visual inspection of the images is not enough to discern any trend of systematically larger values of the M2FR in the presence of AD. To quantify this, we show in Fig. 7 the histograms of the M2FR. The histograms are computed for all LOSs within a circular region centered at $(y, z) = (0, 0)$, with a 20-pc radius. From these, we see that the inclusion of AD causes the production of a small excess of high-M2FR cells in comparison with the non-AD cases, and that this effect is most noticeable in the strong-field (B4) case, in which the maximum value of the M2FR is over a factor of 2 larger than in the non-AD case. Instead, in the B3 case, the excess is marginal, suggesting that when the system is very close to being supercritical, numerical diffusion dominates over AD. This result suggests that the relative importance of AD and numerical diffusion depends on the mean field strength, an issue that deserves further exploration, but which is out of the scope of the present paper.

Returning to Fig. 6, and focusing on the *top row* of images, which show the variation of the M2FR's spatial distribution as a function of the magnetic field strength, several points are worth noting. First, as mentioned above, the M2FR is seen to be highly inhomogeneous in all three runs. This is also illustrated in Fig. 8, whose *top left panel* shows histograms of the M2FR in the three runs at the same time as that shown in Fig. 6. The *top right* and *bottom left* panels of Fig. 8 show the corresponding cumulative distributions, respectively weighted by volume and by mass. Finally, the *bottom right* panel shows the mass-weighted cumulative distribution for high-column density ($N > 10^{21} \text{ cm}^{-2}$) LOSs only. From these figures, it is seen that μ fluctuates by over one order of magnitude in the subcritical runs, and by two in the supercritical one. Part of this variability, especially the highest values of μ , may be an artifact of the measurement procedure, as discussed in Sec. 3.4. Nevertheless, significant actual fluctuations of the M2FR on the plane are expected, since the cloud is turbulent and clumpy, due to the combined action of the thermal, Kelvin-Helmholtz and nonlinear thin-shell (NTSI, Vishniac 1994) instabilities (Vázquez-Semadeni et al. 2006; Heitsch et al. 2006). In the ideal MHD case, segments of magnetic flux tubes must have M2FRs smaller than that of the whole tube at all times. However, in the presence of diffusion (numerical and/or ambipolar), Lagrangian regions where the density is large enough can lose magnetic flux and reach M2FR values larger than the initial value for the

tube. Thus, local clumps may become magnetically supercritical even within the globally subcritical simulations, as in the low-mass mode of the “standard model” of magnetically regulated SF (Shu et al. 1987; Mouschovias 1991), and turbulent extensions of it (Nakamura & Li 2005). According to the *top right* and *bottom left* panels of Fig. 8, the fraction of the volume (resp. mass) that is in locally supercritical regions increases from $\sim 3\%$ (resp. $\sim 10\%$) in run B4-AD to $\sim 17\%$ (resp. $\sim 58\%$) in run B2-AD. In summary, there exist plenty of mechanisms that contribute to the development of a highly inhomogeneous spatial distribution of the M2FR, both in the ideal MHD and in the diffusive cases. This is consistent with recent observational determinations suggesting that the magnetic field strength is randomly distributed in MCs, with only its maximum values scaling as a power law of the density (Crutcher et al. 2010).

Second, we note from the *top left panel* of Fig. 8 that the M2FR histogram for the supercritical run B2-AD is wider than the histograms of either of the subcritical runs, having a larger fraction of *both* sub- and supercritical LOSs. This can be understood as a consequence of the combined action of AD enhanced by turbulence and mass conservation. For weaker magnetic fields, the Alfvénic Mach number is larger, implying larger density fluctuations, in which AD is enhanced (Fatuzzo & Adams 2002; Heitsch et al. 2004; Li & Nakamura 2004), thus allowing the formation of more strongly supercritical clumps, which are denser and contain more mass. In turn, this implies a stronger evacuation of the remaining regions, which are those left with smaller masses, and therefore with lower values of the M2FR.

Third, from the images in Fig. 6, in which the dots indicate the positions of the sink particles, we see that not all of the regions that appear supercritical according to the projection method proceed to form stars. This may be either because they are truly supercritical albeit locally Jeans-stable, or because they are actually magnetically subcritical, and only appear supercritical due to the projection effect. Therefore, it is important to determine the degree to which the M2FR is overestimated by the projection method. We defer a detailed energy-balance study of the clumps and cores for a future paper, but here we can take a first step towards addressing this problem by comparing the maps and histograms of the M2FR obtained with the projection method to those obtained with the “local method” (cf. Sec. 3.4). Figure 9 shows histograms of the M2FR using this method for the middle plane of each simulation at $t = 20$ Myr. Here we do not integrate over any LOS in order to show the largest excursions that the M2FR can exhibit in local cells. As mentioned in Sec. 3.4, the local method gives lower limits to the actual M2FR in the flux tube to which the local cell belongs.

The μ -histograms using the local method exhibit a number of interesting features. First, it is seen that no supercritical cells are seen in both of the subcritical runs. At least for run B3-AD this is necessarily an underestimation of the actual M2FR, since sink formation has already occurred in this run at the time at which the histograms are made ($t = 20$ Myr). Second, the supercritical run B2-AD exhibits a small but finite fraction of supercritical cells, even with this M2FR-underestimating method, indicative of the abundance of supercritical regions in this case. Third, the histograms are seen to peak at $\mu/\mu_{\text{crit}} \sim 10^{-2}$, while those obtained with the projection method peak at $\mu/\mu_{\text{crit}} \sim 0.6$.

Thus, the difference between the two methods is so large that the true distribution remains relatively unconstrained between them.

A final criterion that can be used to determine the accuracy of the observational-like projection method is to compare the supercritical mass fraction obtained with this method with the SFE, which is in fact a measure of the mass fraction that has become simultaneously Jeans-unstable and magnetically supercritical over the cloud's history. Unfortunately, in principle this relationship is not trivial, because the supercritical mass fraction is an instantaneous quantity in the simulation, while the stellar mass in the cloud is a time-integrated quantity. However, if an approximately stationary state is established in which fresh gas is continuously added to the clouds by accretion from the WNM, replenishing the gas used up to form stars (Vázquez-Semadeni et al. 2010), then the (stationary) SFE may be considered as a lower limit to the (stationary) supercritical mass fraction. The notion that the SFE is a lower limit of the supercritical mass fraction allows for the possibility that efficiency of conversion of gas to stars is still less than unity even within the supercritical, Jeans-unstable gas.

With this in mind, we plot in Fig. 10 the SFE versus the supercritical mass fraction in the three runs B2-AD, B3-AD and B4-AD, as read off from Figs. 5 (*bottom right* panel) and 8 (*bottom left* panel). The plotted value of the SFE is the mean between the extremes taken by the SFE over the time interval after which the initial rapid growth has ended, and the error bars denote these extremes. The dotted line indicates a least squares fit to the data points, given by

$$\text{SFE} \approx -0.034 + 0.54 \left(\frac{M_{\text{sup}}}{M} \right). \quad (8)$$

Of course, this fit is totally empirical, and is provided only as a guideline for the trend of the SFE with the supercritical mass fraction. In particular, it is meaningless below the value of the supercritical mass fraction that produces an SFE of zero.

We observe that, in all three cases, the SFE is a few to several times smaller than the supercritical mass fraction. Under the assumption of stationarity, this then suggests that the supercritical mass fraction obtained through the projection method does not differ from the real one by more than factors of a few, on average.

A final point worth noting is that, as shown in the *bottom right* panel of Fig. 8, the supercritical mass fraction in the high-column density gas is significantly larger in all three runs than the supercritical mass fraction for gas at all column densities (*bottom left* panel). This reinforces the scenario that the M2FR is determined mainly by the column density acquired by the individual regions in the clouds by accretion of gas along field lines, and less importantly by the local effect of ambipolar (and/or numerical) diffusion.

We conclude from this section that the projection method gives estimates of the M2FR that are within less than a factor of a few from the actual distribution, and that the dominant mechanism that determines the local M2FR is the accumulation of gas along field lines.

4.3 Evolution of the global M2FR

We proceed now to discuss the evolution of the mean M2FR of the clouds in the simulations, and its range of variability. Figure 11 shows the evolution of the mean and the 3σ range of the normalized M2FR, μ/μ_{crit} , for runs B2-AD (*top* panels), B3-AD (*middle* panels), and B4-AD (*bottom* panels). The computation of the M2FR is performed using the projection method with the same path length and over the same circular region as those used for the histograms of Fig. 8. The *left* panels of Fig. 11 show the mean and 3σ range computed for the set of all lines of sight contained in the circular region, while the *right* panels show these quantities computed only for the set of lines of sight for which the column density is larger than 10^{21} cm^{-2} .

These plots illustrate the fact, discussed in Sec. 2, that the M2FR of a cloud is an evolving quantity, which first increases as the cloud gathers material from the WNM inflows that assemble it. At the inflow speed of 13.9 km s^{-1} , the 112-pc-long inflows are entirely incorporated into the cloud in approximately 8 Myr, which indeed corresponds to the time scale at which the M2FR of all three clouds is seen to have reached a roughly stationary value. This value is seen to be larger for weaker mean field, as expected. However, a second increase in the M2FR is seen to occur after this first stabilization. This can be attributed to the fact that the inflows drag part of the surrounding, initially static WNM along with them, as they leave a partial vacuum behind them. This dragged material flows at lower speeds, and reaches the cloud at later times (for further discussion, see Vázquez-Semadeni et al. 2007).

It is interesting that $\langle \mu/\mu_{\text{crit}} \rangle$ for the set of all lines of sight is smaller than unity at all times for all three runs, even the supercritical one, B2-AD. This is likely a consequence of mass conservation again (cf. Sec. 4.2). Because these statistics are weighted by area over the circular region, the supercritical regions, which are denser, occupy a smaller fraction of the surface area of the cloud, and therefore the area-weighted average M2FR is smaller than unity in all cases. However, the averages for the high-column density LOSs, shown in the *right panels* of Fig. 11 are larger than unity for all times in run B2-AD, and for nearly 20 Myr in run B3-AD. Instead, for run B4-AD, even this high- N average barely reaches values larger than unity, and only over less than 10 Myr. Finally, in all cases, the high- N average M2FR decreases at late times, a phenomenon that can be attributed to the high-M2FR gas consumption by star formation.

In general, we conclude from Sections 4.2 and 4.3 that the M2FR is a time-dependent function of time as a cloud is built up by converging WNM streams, whose average generally increases with time, although in the high- N regions the average later decays due to consumption by SF. Spatially, the M2FR exhibits large fluctuations, whose $3\text{-}\sigma$ range spans over one order of magnitude even in the strong-field cases. It is the high-M2FR tail of the distribution that is responsible for star formation.

4.4 Buoyancy of subcritical regions

An unexpected feature we have observed in these simulations is that the subcritical and supercritical regions do not

maintain their relative positions fixed throughout the evolution of the simulations. Instead, the subcritical regions exhibit “buoyancy”, so that they tend to separate themselves from the global contraction of the clouds, even in the globally subcritical cases that rebound at later times. This is most clearly seen in animations of the simulations, but can be seen in Fig. 12, where we show that, as time proceeds, the subcritical regions become segregated from the supercritical ones, moving outwards, and developing cometary shapes, with their heads pointing outwards as well.

This behavior can be described as a macroscopic-scale analogue of the very process of AD. In the latter, the neutrals sink into the gravitational potential well, percolating through the ions, which remain attached to the magnetic field lines. In our case, the supercritical regions sink into the potential well, while the subcritical ones remain in the outer parts of the well, being held up by the magnetic tension. The process is also reminiscent of the interchange mode of the Parker instability (Hughes & Cattaneo 1987).

5 SUMMARY AND CONCLUSIONS

In this paper we have presented a study of the formation and evolution of GMCs by the convergence of WNM streams, or “inflows”, in the presence of magnetic fields and AD. As described by many groups (see the review by Vázquez-Semadeni 2010, and references therein), this process involves the transition of the atomic gas from the warm, diffuse phase to the cold, dense one, allowing the fresh cold gas to quickly become self-gravitating and begin to contract.

We first reviewed the general evolution of the gas and the M2FR expected in this type of systems, noting that, as originally pointed out by Hartmann et al. (2001), the mass-to-flux ratio (M2FR) of the cloud is expected to increase in time, so that the cloud becomes molecular, self-gravitating, and magnetically supercritical at roughly the same time, provided that there is enough mass in the converging streams to render them supercritical. This condition requires that, for solar neighborhood conditions, the inflows extend beyond the accumulation length given by eq. (2). Flows that do not extend to such distances are expected to form subcritical clouds which, however, may be predominantly atomic. This suggests that, in particular, the converging flows induced by the spiral-arm potential wells, which have typical size scales ~ 1 kpc, will in general induce the formation of magnetically supercritical molecular clouds. On the other hand, converging flows induced by smaller-scale inflows, such as supernova shocks, or simply turbulent random motions in the gas, may lead to the formation of subcritical, partially atomic clouds.

We then discussed the difficulties inherent to measuring the M2FR, even under controlled conditions such as those of the simulations. Other than measuring the M2FR along magnetic flux tubes, which is impossible to perform observationally, and perhaps even numerically, we considered two methods for measuring the M2FR: the “projection” method, which mimicks the observational procedure of measuring the ratio of column density to field strength along the line of sight (LOS), and which gives an upper limit to the actual M2FR, and the “local” method, which simply measures the mass and magnetic field in a grid cell in the simulation, and

estimates the M2FR as given by eq. (6), giving a lower limit to the M2FR.

We next studied the evolution of the M2FR and the star-forming properties of clouds formed by both sub- and supercritical inflows. We concluded that in our simulations, the effect of numerical diffusion is at a comparable level to that of AD. We found that the subcritical cases do undergo an initial phase of contraction, followed by a re-expansion, settling into an oscillatory regime. The supercritical case, on the other hand, proceeds directly to collapse, as expected. All cases form stars, although at greatly different rates, producing what appears more a continuum of star-forming regimes as the mean magnetic field strength is varied, rather than a bimodal regime of high SFR in supercritical cases and low SFR in subcritical ones, as was the case in the “standard” model of magnetically regulated SF (Shu et al. 1987; Mouschovias 1991). In particular, the marginally subcritical case B3-AD, through the action of diffusion, reached SF efficiencies (SFEs) comparable to those of the supercritical case B2-AD. The onset of SF is delayed by up to 15 Myr in the most strongly magnetized cases we studied, although this delay is reduced by a few to several Myr when AD is included (when it is not, all SF activity is due to numerical diffusion). The SFEs observed in our simulations range from $\sim 35\%$ for run B2-AD to $\sim 3\%$ for run B4-AD. However, since stellar feedback, which would reduce the SFE even further, is not included in these simulations, it is likely that the efficiency of run B4-AD is actually too low in comparison with observed values.

We then investigated the spatial and statistical distribution of the M2FR, finding that this is a highly fluctuating quantity. The fragmentation of the cloud by the combined action of thermal, nonlinear thin-shell, and gravitational instabilities leads to the formation of clumps of high density and high M2FR, and of low-density, low-M2FR patches. The fluctuations in the M2FR we observed span between one-and-a-half and two orders of magnitude, the distribution being wider for weaker magnetizations. These results are qualitatively consistent with recent observational determinations suggesting that the magnetic field strength in MCs is strongly fluctuating (Crutcher et al. 2010).

Next, we discussed the evolution of the mean M2FR and its 3σ range in the various simulations, finding that in general it initially increases as expected by the assembly process of the cloud, to later reach a roughly stationary regime. The M2FR of the high-column-density LOSs, on the other hand, tends to decrease at later times, due to the consumption of gas in this regime by SF.

Finally, we reported the occurrence of an unexpected effect: the buoyancy of the low-M2FR regions with respect to the high-M2FR ones, through a process that appears as the macroscopic-scale analogue of AD: the high-M2FR regions sink deeper into the potential well of the cloud, while the low-M2FR ones remain supported by the field in the outer parts of the cloud, so that the clouds evolve towards a segregated state with low M2FR in their periphery and high-M2FR towards their centre, even on scales much larger, and densities much lower than, those directly affected by AD. The process also bears resemblance with the interchange mode of the Parker instability.

ACKNOWLEDGMENTS

The FLASH code was developed in part by the DOE-supported Alliances Center for Astrophysical Thermonuclear Flashes (ASC) at the University of Chicago. Our simulations were carried out at the Leibniz Rechenzentrum, Garching and the Jülich Supercomputing Centre (JSC). We gratefully acknowledge the following sources of financial support: CONACYT (México) grants U47366-F and 102488 to E.V.-S.; Emmy-Noether (DFG) grant BA 3706 to R.B.; International Collaboration II (grant P-LS-SPII/18) program of the Landesstiftung Baden-Württemberg, subsidies from the Deutsche Forschungsgemeinschaft under grants no. KL 1358/1, KL 1358/4, KL 1359/5, KL 1358/10, and KL 1358/11, and a Frontier grant of Heidelberg University sponsored by the German Excellence Initiative to R.S.K.

REFERENCES

- Audit, E. & Hennebelle, P. 2005, *A&A* 433, 1
- Ballesteros-Paredes, J., Klessen, R. S., Mac Low, M.-M., & Vázquez-Semadeni, E. 2007, *Protostars and Planets V*, 63
- Ballesteros-Paredes, J., Hartmann, L., & Vázquez-Semadeni, E. 1999, *ApJ*, 527, 285
- Ballesteros-Paredes, J., Klessen, R. S., & Vázquez-Semadeni, E. 2003, *ApJ*, 592, 188
- Ballesteros-Paredes, J., Vázquez-Semadeni, E., & Scalo, J. 1999, *ApJ*, 515, 286
- Banerjee, R., Vázquez-Semadeni, E., Hennebelle, P., & Klessen, R. S. 2009, *MNRAS*, 398, 1082
- Basu, S., & Mouschovias, T. C. 1994, *ApJ*, 432, 720
- Bate, M. R., Bonnell, I. A., & Price, N. M. 1995, *MNRAS*, 277, 362
- Beck, R. 2001, *Sp. Sci. Rev.* 99, 243
- Bergin, E. A., Hartmann, L. W., Raymond, J. C., & Ballesteros-Paredes, J. 2004, *ApJ*, 612, 921
- Bertoldi, F., & McKee, C. F. 1992, *ApJ*, 395, 140
- Bonazzola, S., Heyvaerts, J., Falgarone, E., Pérault, M., & Puget, J. L. 1987, *A&A*, 172, 293
- Bourke, T. L., Myers, P. C., Robinson, G., & Hyland, A. R. 2001, *ApJ*, 554, 916
- Chandrasekhar, S. 1951, *Royal Society of London Proceedings Series A*, 210, 26
- Ciolek, G. E., & Basu, S. 2001, *ApJ*, 547, 272
- Ciolek, G. E., & Basu, S. 2001, *ApJ*, 547, 272
- Ciolek, G. E., & Mouschovias, T. C. 1994, *ApJ*, 425, 142
- Crutcher, R. M. 1999, *ApJ*, 520, 706
- Crutcher, R., Heiles, C., & Troland, T. 2003, *Turbulence and Magnetic Fields in Astrophysics*, 614, 155
- Crutcher, R. M., Wandelt, B., Heiles, C., Falgarone, E., & Troland, T. H. 2010, *ApJ*, 725, 466
- Csengeri, T., Bontemps, S., Schneider, N., Motte, F., & Dib, S. 2010, *A&A* in press (arXiv:1009.0598)
- Diehl, R., et al. 2006, *Nature*, 439, 45
- Duffin, D. F., & Pudritz, R. E. 2008, *MNRAS*, 391, 1659
- Elmegreen, B. G. 2007, *ApJ*, 668, 1064
- Elmegreen, B. G., & Scalo, J. 2004, *ARAA*, 42, 211
- Evans, N. J., et al. 2009, *ApJS*, 181, 321
- Fatuzzo, M., & Adams, F. C. 2002, *ApJ*, 570, 210
- Federrath, C., Banerjee, R., Clark, P. C., & Klessen, R. S. 2010, *ApJ*, 713, 269
- Field, G. B., Blackman, E. G., & Keto, E. R. 2008, *MNRAS*, 385, 181
- Franco, J., & Cox, D. P. 1986, *PASP*, 98, 1076
- Fryxell, B., et al. 2000, *ApJS*, 131, 273
- Fukui, Y., et al. 2009, *ApJ*, 705, 144
- Galván-Madrid, R., Keto, E., Zhang, Q., Kurtz, S., Rodríguez, L. F., & Ho, P. T. P. 2009, *ApJ*, 706, 1036
- Galván-Madrid, R., Vázquez-Semadeni, E., Kim, J., & Ballesteros-Paredes, J. 2007, *ApJ*, 670, 480
- Glover, S. C. O., Federrath, C., Mac Low, M.-M., & Klessen, R. S. 2010, *MNRAS*, 404, 2
- Glover, S. C. O., & Mac Low, M.-M. 2007, *ApJ*, 659, 1317
- Glover, S. C. O., & Mac Low, M.-M. 2007, *ApJS*, 169, 239
- Hartmann, L., Ballesteros-Paredes, J., & Bergin, E. A. 2001, *ApJ*, 562, 852
- Hartmann, L. & Burkert, A. 2007, *ApJ*, 654, 988
- Heiles, C., & Troland, T. H. 2005, *ApJ*, 624, 773
- Heitsch, F., & Hartmann, L. 2008, *ApJ*, 689, 290
- Heitsch, F., Burkert, A., Hartmann, L., Slyz, A. D., & Devriendt, J. E. G. 2005, *ApJ* 633, L113
- Heitsch, F., Mac Low, M.-M., & Klessen, R. S. 2001, *ApJ*, 547, 280
- Heitsch, F., Slyz, A. D., Devriendt, J. E. G., Hartmann, L. W., & Burkert, A. 2006, *ApJ*, 648, 1052
- Heitsch, F., Zweibel, E. G., Slyz, A. D., & Devriendt, J. E. G. 2004, *ApJ*, 603, 165
- Hennebelle, P., Banerjee, R., Vázquez-Semadeni, E., Klessen, R. S., & Audit, E. 2008, *A&A*, 486, L43
- Hennebelle, P., Mac Low, M.-M., & Vázquez-Semadeni, E. 2009, *Structure Formation in Astrophysics*, ed. G. Chabrier (Cambridge: Cambridge University Press), 205
- Hennebelle, P. & Pérault, M. 1999, *A&A* 351, 309
- Hennebelle, P., & Pérault, M. 2000, *A&A*, 359, 1124
- Heyer, M., Gong, H., Ostriker, E., & Brunt, C. 2008, *ApJ*, 680, 420
- Hughes, D. W., & Cattaneo, F. 1987, *Geophysical and Astrophysical Fluid Dynamics*, 39, 65
- Hunter, J. H., Jr., Sandford, M. T., II, Whitaker, R. W., & Klein, R. I. 1986, *ApJ*, 305, 309
- Jappsen, A.-K., Klessen, R. S., Larson, R. B., Li, Y., & Mac Low, M.-M. 2005, *A&A*, 435, 611
- Kim, W.-T., Ostriker, E. C., & Stone, J. M. 2003, *ApJ*, 599, 1157
- Kim, W.-T., & Ostriker, E. C. 2007, *ApJ*, 660, 1232
- Kirk, H., Johnstone, D., & Di Francesco, J. 2006, *ApJ*, 646, 1009
- Klessen, R. S., Ballesteros-Paredes, J., Vázquez-Semadeni, E., & Durán-Rojas, C. 2005, *ApJ*, 620, 786
- Klessen, R. S., Heitsch, F., & Mac Low, M.-M. 2000, *ApJ*, 535, 887
- Klessen, R. S., & Hennebelle, P. 2010, *A&A*, 520, A17
- Kolmogorov, A. 1941, *Akademiia Nauk SSSR Doklady*, 30, 301
- Koyama, H., & Inutsuka, S.-I. 2000, *ApJ*, 532, 980
- Koyama, H. & Inutsuka, S.-I. 2002, *ApJ*, 564, L97
- Lada, C. J., & Lada, E. A. 2003, *ARAA*, 41, 57
- Li, Y., Mac Low, M.-M., & Klessen, R. S. 2005, *ApJ*, 626, 823
- Li, Z.-Y., Nakamura, F. 2004, *ApJ*, 609, L83
- Mac Low, M.-M., & Klessen, R. S. 2004, *Reviews of Modern Physics*, 76, 125
- McKee, C. F. 1989, *ApJ*, 345, 782

- McKee, C. F., & Ostriker, E. C. 2007, *ARAA*, 45, 565
- Mestel, L. 1985, *Protostars and Planets II*, 320
- Mestel, L., & Spitzer, L., Jr. 1956, *MNRAS*, 116, 503
- Mouschovias, T. C. 1977, *ApJ*, 211, 147
- Mouschovias, T. C. 1991, *NATO ASIC Proc. 342: The Physics of Star Formation and Early Stellar Evolution*, 449
- Mouschovias, T. C., Paleologou, E. V., & Fiedler, R. A. 1985, *ApJ*, 291, 772
- Mouschovias T. C., Spitzer Jr. L., 1976, *ApJ*, 210, 326
- Myers, P. C., Dame, T. M., Thaddeus, P., Cohen, R. S., Silverberg, R. F., Dwek, E. & Hauser, M. G. 1986, *ApJ*, 301, 398
- Myers, P. C., & Goodman, A. A. 1988, *ApJ*, 326, L27
- Nakamura, F., & Li, Z.-Y. 2005, *ApJ*, 631, 411
- Nakano, T., & Nakamura, T. 1978, *PASJ*, 30, 671
- Ostriker, E. C., Gammie, C. F., & Stone, J. M. 1999, *ApJ*, 513, 259
- Peretto, N., Hennebelle, P., André, P. 2007, *A&A*, 464, 983
- Pittard, J. M., Dobson, M. S., Durisen, R. H., Dyson, J. E., Hartquist, T. W., & O'Brien, J. T. 2005, *A&A*, 438, 11
- Schneider, N., Csengeri, T., Bontemps, S., Motte, F., Simon, R., Hennebelle, P., Federrath, C., & Klessen, R. 2010, *A&A*, 520, A49
- Shu, F. H. 1992, *Physics of Astrophysics*, Vol. II, by Frank H. Shu. Published by University Science Books
- Shu, F. H., Adams, F. C., & Lizano, S. 1987, *ARAA*, 25, 23
- Shu, F. H., Allen, R. J., Lizano, S., & Galli, D. 2007, *ApJ*, 662, L75
- Troland, T. H., & Crutcher, R. M. 2008, *ApJ*, 680, 457
- Truelove, J. K., Klein, R. I., McKee, C. F., Holliman, J. H., II, Howell, L. H., & Greenough, J. A. 1997, *ApJ*, 489, L179
- van Dishoeck, E. F., & Black, J. H. 1988, *ApJ*, 334, 771
- van Dishoeck, E. F., & Blake, G. A. 1998, *ARAA*, 36, 317
- Vázquez-Semadeni, E. 2009, arXiv:0902.0820
- Vázquez-Semadeni, E. 2010, in "The Dynamic ISM: A celebration of the Canadian Galactic Plane Survey", ed. R. Kothes, in press (arXiv:1009.3962)
- Vázquez-Semadeni, E., & Gazol, A. 1995, *A&A*, 303, 204
- Vázquez-Semadeni, E., Colín, P., Gómez, G. C., Ballesteros-Paredes, J., Watson, A. W. 2010, *ApJ*, 715, 1302
- Vázquez-Semadeni, E., Gazol, A., Passot, T., & et al. 2003, *Turbulence and Magnetic Fields in Astrophysics*, 614, 213
- Vázquez-Semadeni, E., Gómez, G. C., Jappsen, A. K., Ballesteros-Paredes, J., González, R. F., & Klessen, R. S. 2007, *ApJ*, 657, 870 (Paper I)
- Vázquez-Semadeni, E., Gómez, G. C., Jappsen, A.-K., Ballesteros-Paredes, J., & Klessen, R. S. 2009, *ApJ*, 707, 1023
- Vázquez-Semadeni, E., González, R. F., Ballesteros-Paredes, J., Gazol, A., Kim, J. 2008, *MNRAS*, 390, 769
- Vázquez-Semadeni, E., Kim, J., Shadmehri, M., & Ballesteros-Paredes, J. 2005, *ApJ*, 618, 344
- Vázquez-Semadeni, E., Ostriker, E. C., Passot, T., Gammie, C. F., & Stone, J. M. 2000, *Protostars and Planets IV*, 3
- Vázquez-Semadeni, E., Ryu, D., Passot, T., González, R. F., & Gazol, A., 2006, *ApJ*, 643, 245
- Vishniac, E. T. 1994, *ApJ*, 428, 186
- Walder, R., & Folini, D. 2000, *Ap&SS*, 274, 343
- Zuckerman, B. & Palmer, P. 1974, *ARA&A*, 12, 279

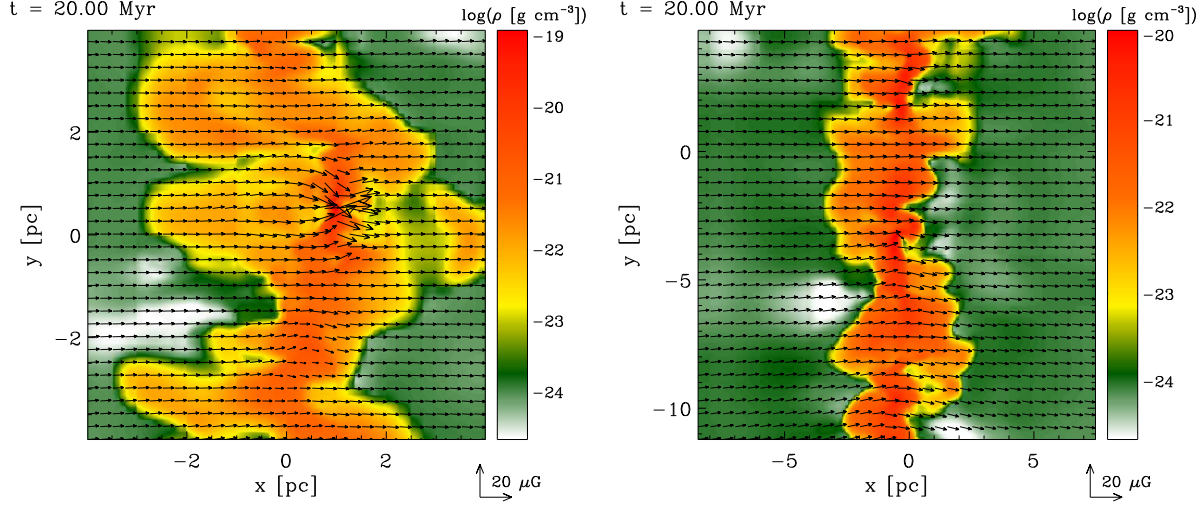


Figure 1. Cross section through the simulation centre on the (x, y) plane, showing the density field on the plane and the component of the magnetic field on this plane, for the B3-MH (*left panel*) and for the B4-MH (*right panel*) runs at $t = 20$ Myr. The initial flow collision occurred along the x direction, which is also the direction of the mean magnetic field.

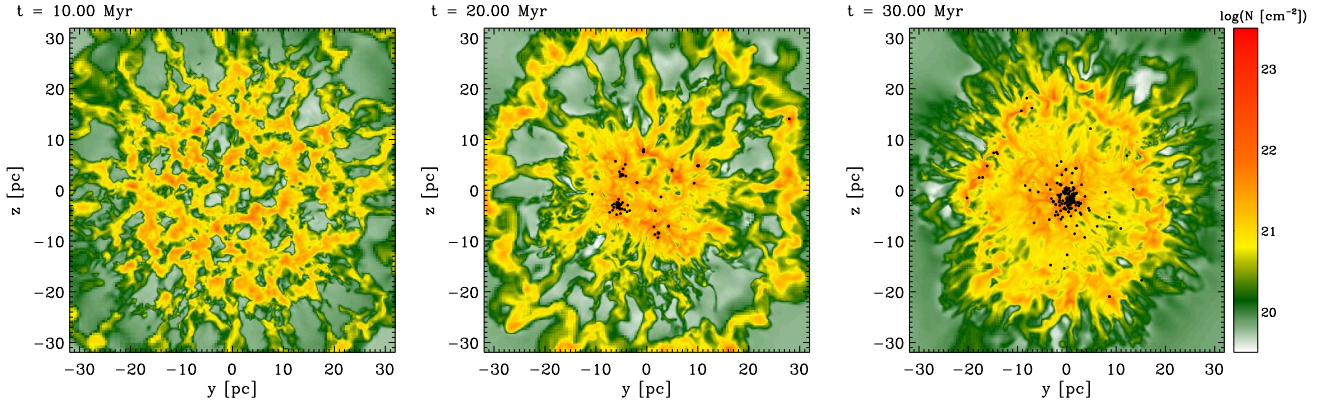


Figure 2. Snapshots of run B2-AD showing the column density integrated along the central 20 parsecs of the simulation along the x -direction (perpendicular to the colliding inflows), at times $t = 10$ Myr (*left panel*), $t = 20$ Myr (*middle panel*), and $t = 30$ Myr (*right panel*).

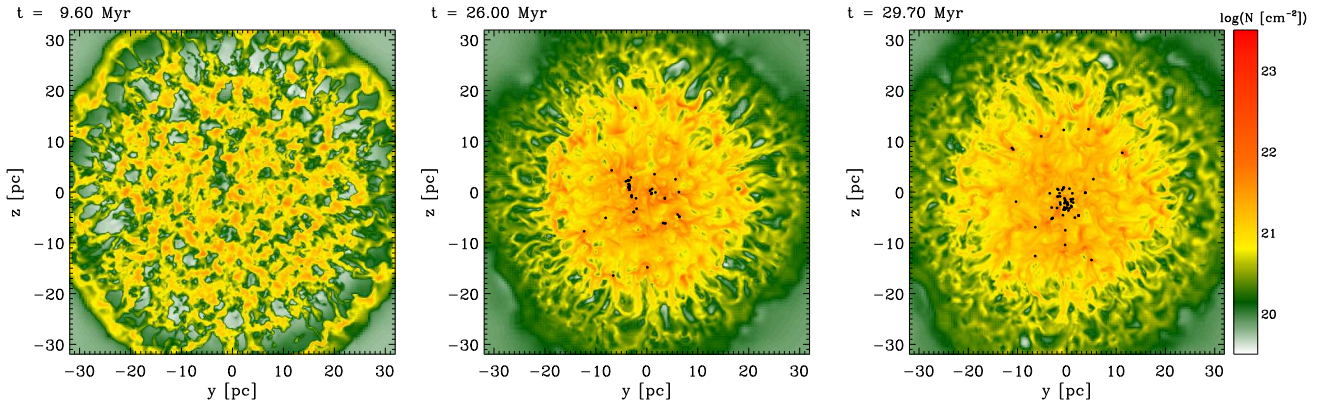


Figure 3. Snapshots of run B3-AD showing the column density integrated along the central 20 parsecs of the simulation along the x -direction (perpendicular to the colliding inflows), at times $t = 9.6$ Myr (*left panel*), $t = 26$ Myr (*middle panel*), and $t = 29.7$ Myr (*right panel*). The simulation contracts until $t = 26$ Myr, after which it begins to rebound.

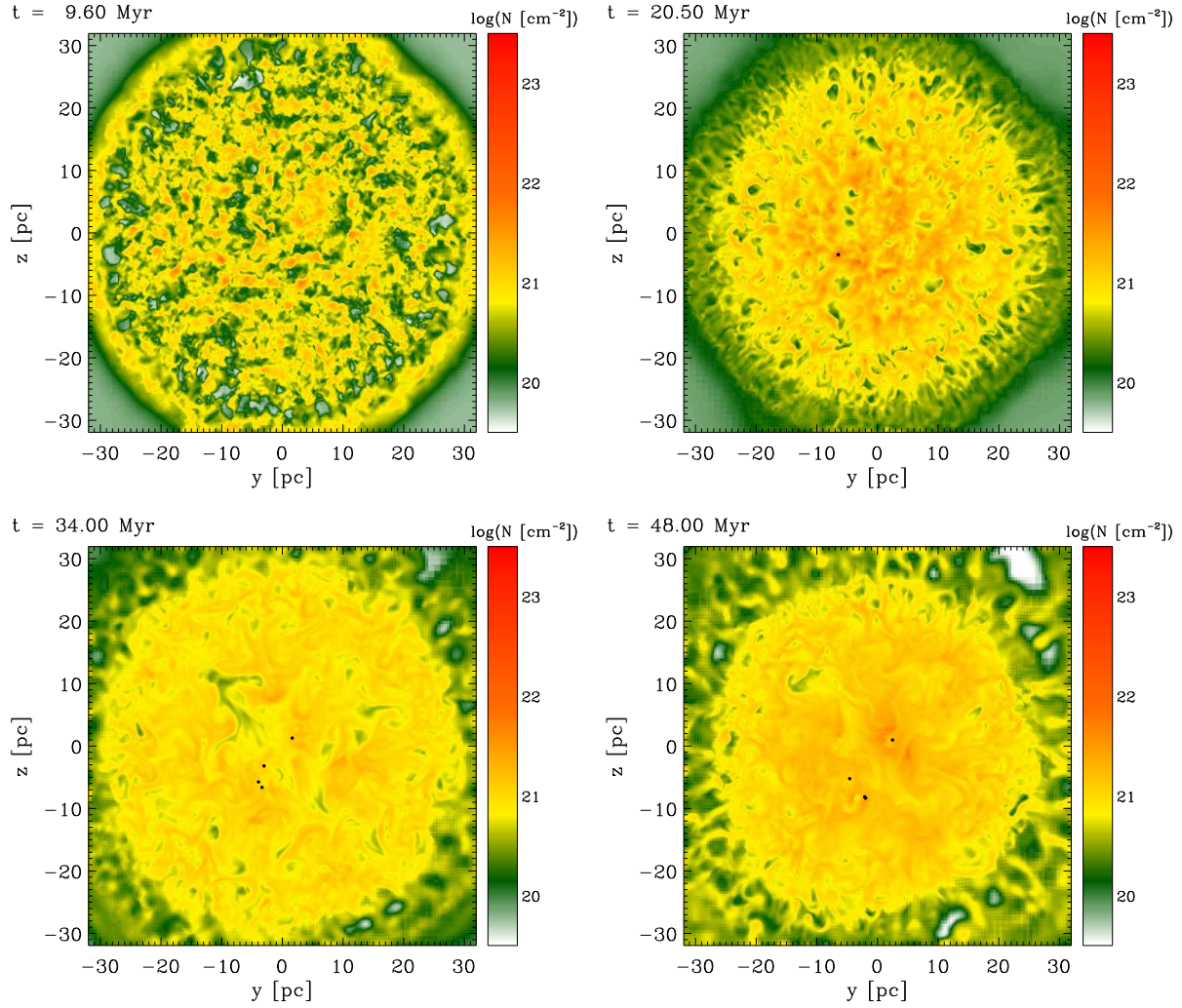


Figure 4. Snapshots of run B4-AD showing the column density integrated along the central 20 parsecs of the simulation along the x -direction (perpendicular to the colliding inflows), at times $t = 9.6$ Myr (*top left panel*), $t = 20.5$ Myr (*top right panel*), $t = 34$ Myr (*bottom left panel*), and $t = 48$ Myr (*bottom right panel*). The simulation is seen to be undergoing global oscillations, with star formation (indicated by the dots) scarcely occurring only during the times of maximum compression.

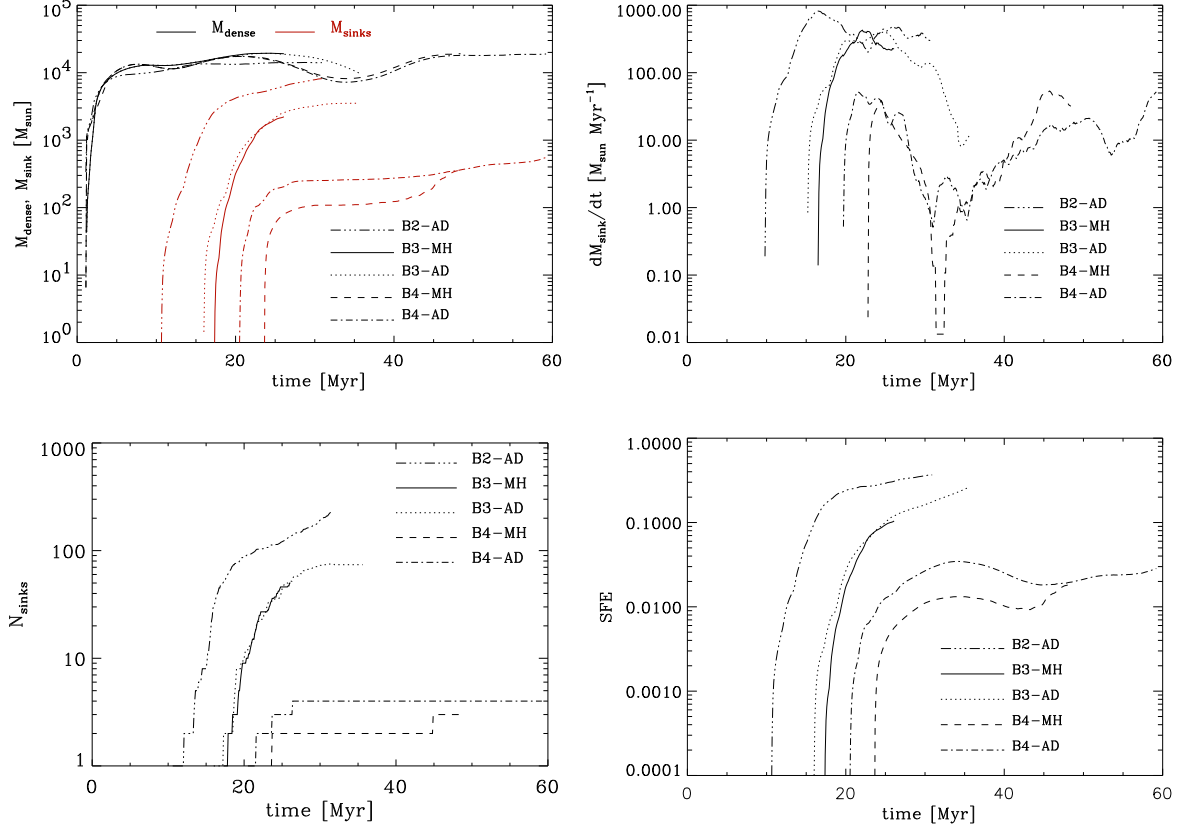


Figure 5. Evolution of the total dense gas mass ($n > 100 \text{ cm}^{-3}$) and total sink mass (*top left panel*), the time derivative of the total sink mass M_{sinks} (approximately giving the SFR; *top right panel*), the total number of sink particles (*bottom left panel*), and the SFE, defined by eq. (7) (*bottom right panel*) in all simulations. The density range for the dense gas includes gas that would classify as “atomic” as well as “molecular”. The graphs of \dot{M}_{sinks} have been smoothed by averaging over 16 neighboring data points at each plotted value.

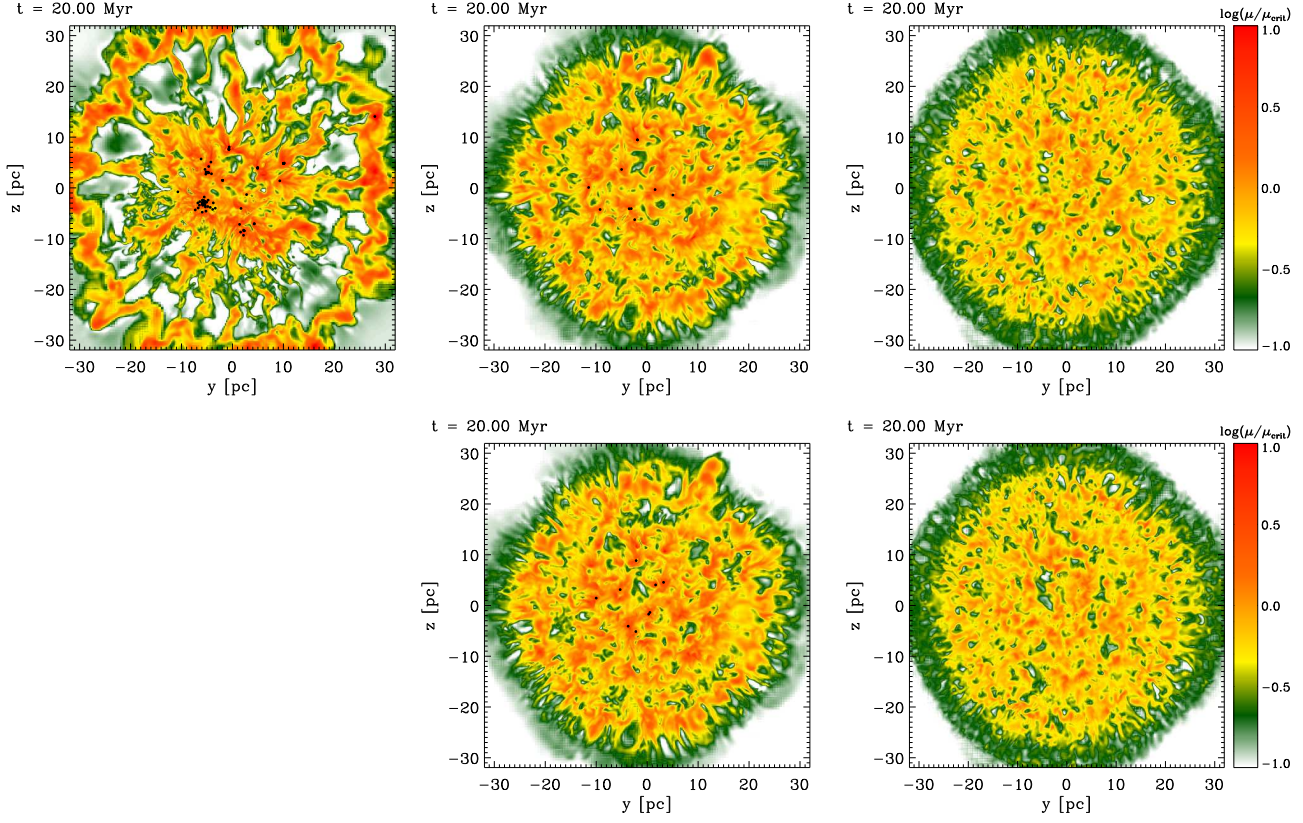


Figure 6. Snapshots of the mass-to-flux ratio μ , normalized to the critical value, for runs B2-AD (*top left panel*), B3-AD (*top middle panel*), B4-AD (*top right panel*), B3-MH (*bottom middle panel*) and B4-MH (*bottom right panel*) at time $t = 20$ Myr. The M2FR is calculated as N/B_{LOS} , as indicated by eq. (5), integrated over a 20-pc path centered at the midplane of the simulation along the direction of the inflows. This path completely encloses the cloud along the x -direction in all simulations. Note that there exist vast numbers of supercritical filaments intermixed with subcritical patches. The latter, however, occupy most of the volume. The dots indicate the positions of sink particles. Note also that the density structure is similar at large scales but different in the small-scale detail between the cases with and without AD.

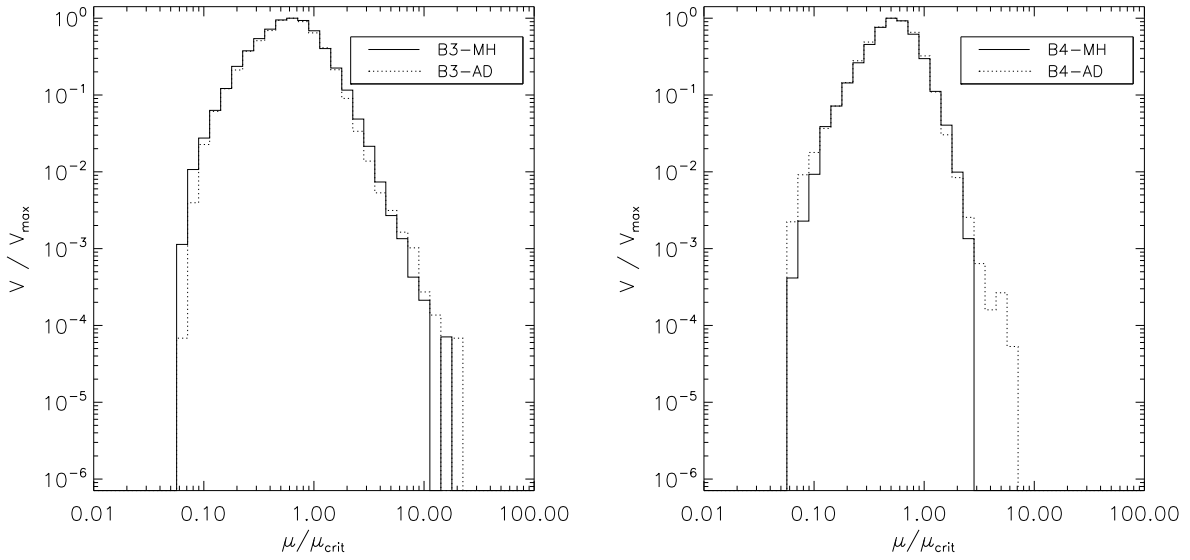


Figure 7. *Left:* Comparison of the M2FR histograms at $t = 20$ Myr, for cases with (*dotted lines*) and without (*solid lines*) AD, for runs B3 (*left panel*), and B4 (*right panel*). The M2FR is estimated through the “projection method”, as indicated by eq. (5) over a circular region centered at the point $(y, z) = (0, 0)$, and of radius 20 pc.

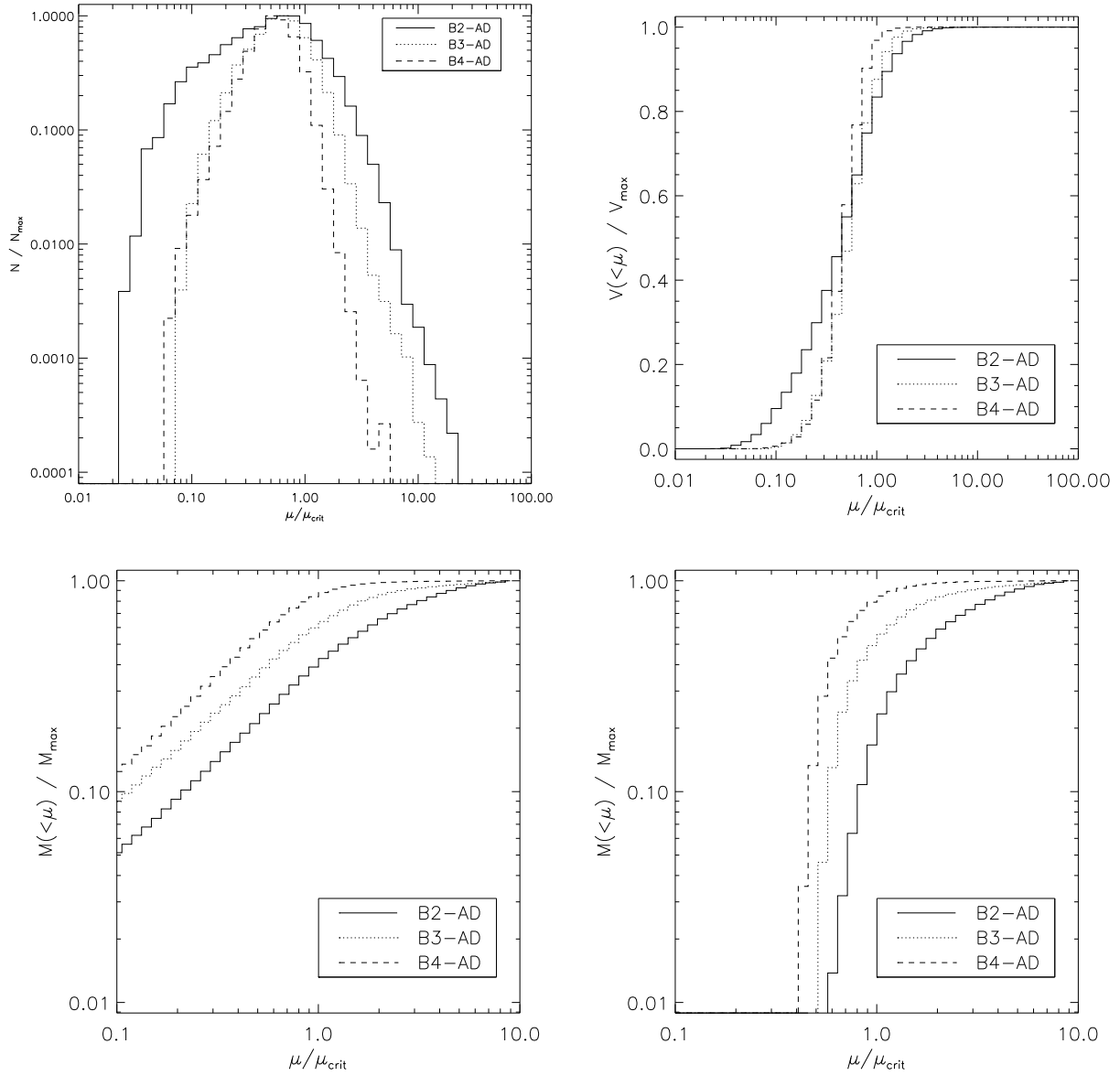


Figure 8. *Top left:* Histograms of the M2FR, estimated through the projection method, for runs B2-AD (solid line), B3-AD (dotted line), and B4-AD (dashed line), at $t = 20$ Myr in all cases. *Top right:* Cumulative probability distributions for the same three runs, with the same line coding. *Bottom left* Density-weighted probability distribution, giving the fraction of mass below the indicated value of μ . *Bottom right* Same as the bottom left panel but for high-column density LOSs ($N > 10^{21} \text{ cm}^{-2}$) only.

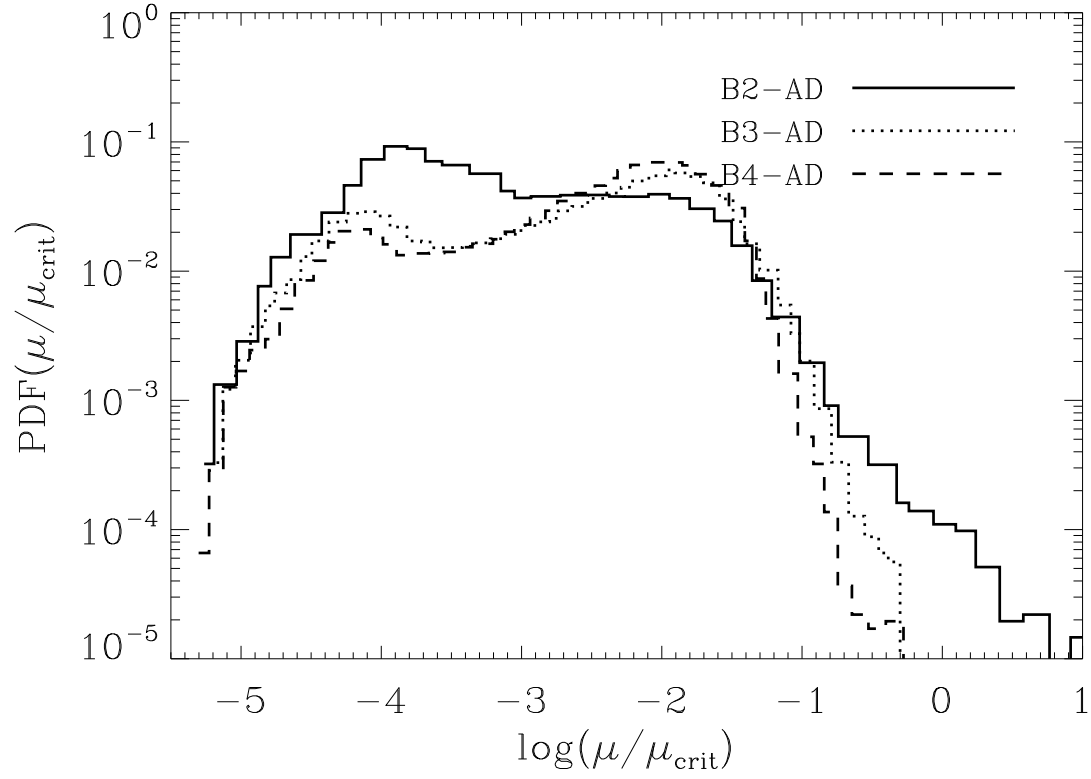


Figure 9. *Left:* Histograms of the M2FR at $t = 20$ Myr, estimated through the “local method”, using eq. (6) for each cell of the middle plane, $x = 0$, of the three simulations, B2-AD (*solid line*), B3-AD (*dotted line*) and B4-AD (*dashed line*). These histograms can be compared to those using the projection method, shown in the *left panel* of Fig. 8.

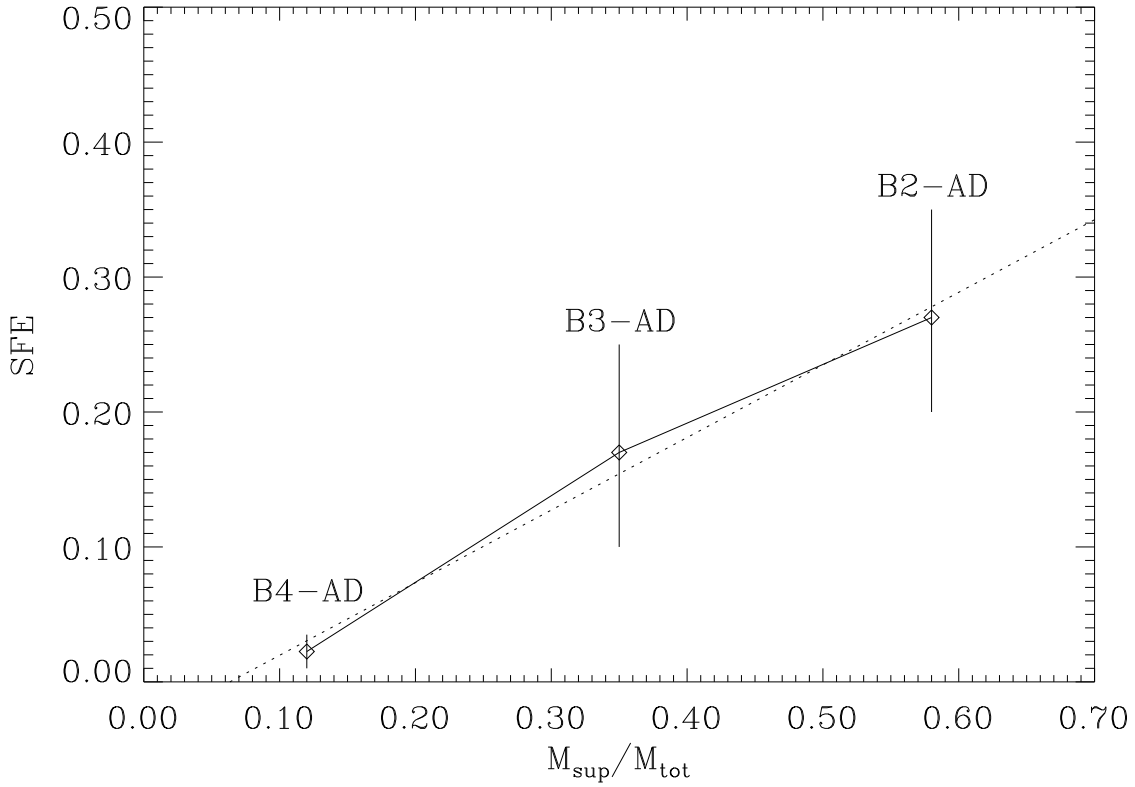


Figure 10. SFE *versus* the supercritical mass fraction in runs B2-AD, B3-AD and B4-AD, with the SFE read off from the *bottom right* panel of Fig. 5 and the supercritical mass fraction read off from the *bottom left* panel of Fig. 8. The plotted value of the SFE is the mean between the extremes taken by the SFE over the time interval after which the initial rapid growth has ended ($18 \lesssim t \leq 26$ Myr for B2-AD, $25 \lesssim t \leq 36$ Myr for B3-AD, and $30 \lesssim t \leq 58$ Myr for B4-AD), and the error bars denote these extremes. The dotted line indicates a least squares fit to the data points, given by eq. (8).

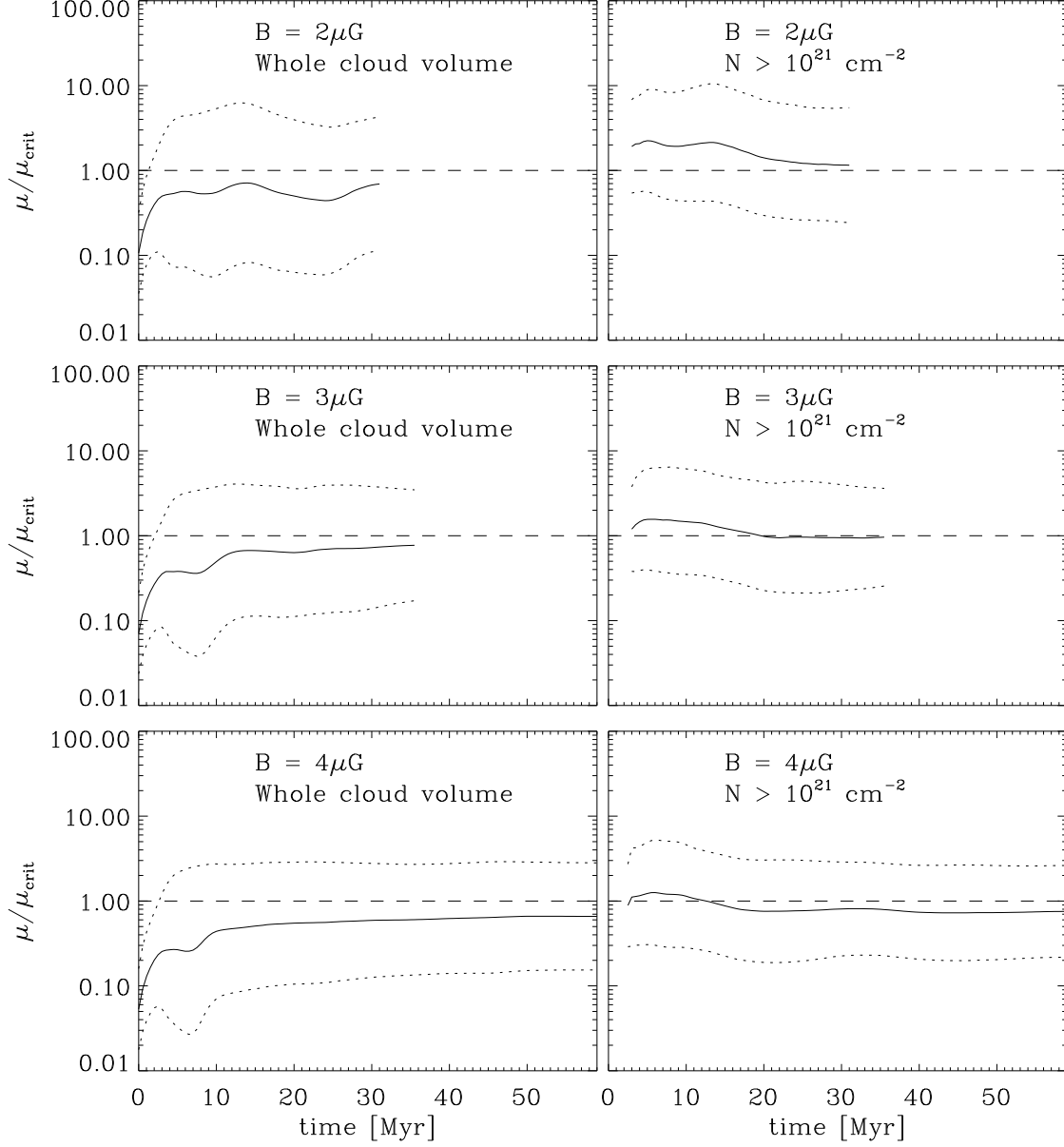


Figure 11. Evolution of the M2FR μ , normalized to the critical value, for runs B2-AD (*top*), B3-AD (*middle*) and B4-AD (*bottom*), computed using the projection method over the same circular region as in Fig. 8. The *solid* lines show the mean value of μ/μ_{crit} , and the *dotted* lines delimit the 3σ range of μ , where the mean and the standard deviation are calculated for $\log \mu$. The *left* panels show these quantities computed for all lines of sight parallel to the axis of a cylindrical volume of length and diameter both equal to 20 pc, centered in the centre of the numerical box. The *right* panels show the same quantities computed only for lines of sight having column densities $N > 10^{21} \text{ cm}^{-2}$. In all cases, the lines of sight extend over the interval $-10 < x < 10$ pc.

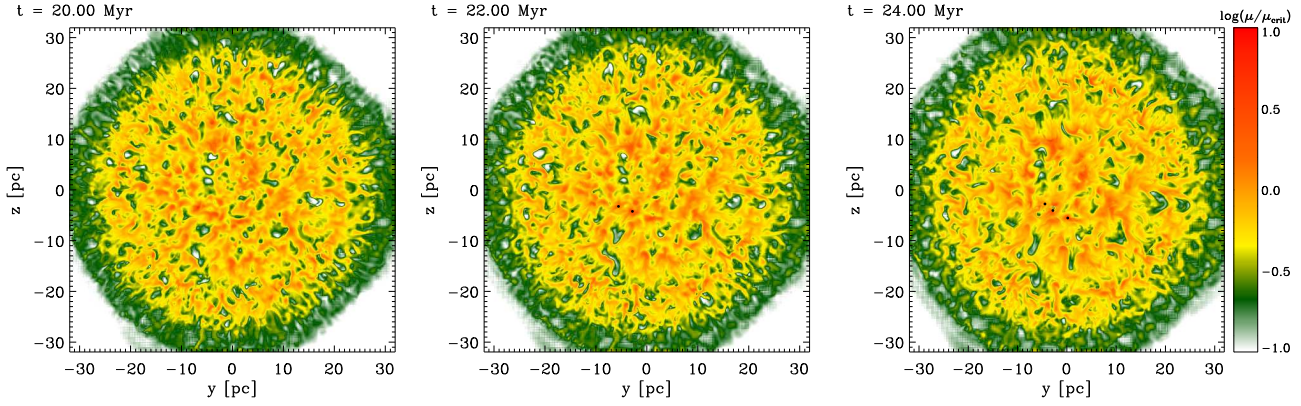


Figure 12. Snapshots of the mass-to-flux ratio μ , normalized to the critical value, for run B4-AD at times $t = 20$ (*left panel*), 22 (*middle panel*), and 24 (*right panel*) Myr. Note the evolution of the subcritical regions, shown in green, which develop cometary shapes, pointing outwards from the centre of the image.